ACS OMEGA

http://pubs.acs.org/journal/acsodf

Article

Synthesis, Characterization, Crystal Structure, DNA and HSA Interactions, and Anticancer Activity of a Mononuclear Cu(II) Complex with a Schiff Base Ligand Containing a Thiadiazoline Moiety

Sidhali U. Parsekar,[§] Kumudini Paliwal,[§] Paramita Haldar, P. K. Sudhadevi Antharjanam, and Manjuri Kumar*

Cite This: *ACS Omega* 2022, 7, 2881−2896

Read Online

ACCESS | Metrics & More | Article Recommendations | Supporting Information

ABSTRACT: A mononuclear Cu(II) complex [Cu(HL)(*o*-phen)]·H_2O (**1**) [H_3L = *o*-HOC$_6$H$_4$–C(H)=N–N=C–S–C(=N–NH)–C$_6$H$_4$OH-*o*, *o*-phen = 1,10-phenanthroline] was isolated from methanol, and its X-ray single-crystal structure was determined. Frozen glass X-band EPR of **1** in dimethylformamide (DMF) at LNT showed a spectrum that is characteristic of a monomeric tetragonal character with $g_{\|}$ = 2.164, $g_{\perp}$ = 2.087, $A_{\|}$ = 19.08 mT, and $A_{\perp} \leq 4$ mT. Electronic spectroscopic studies using calf thymus DNA (CT-DNA) showed strong binding affinity of **1** as reflected from its intrinsic binding constant (K_b) value of 2.85 × 10^5 M^{-1}. Competitive behavior of **1** with ethidium bromide (EB) displayed intercalative binding of DNA (K_{app} = 1.3 × 10^6 M^{-1}). The compound displayed significant oxidative cleavage of pUC19 DNA. The interaction between HSA and complex **1** was examined by employing fluorescence and electronic absorption spectroscopic experiments. The secondary and tertiary structures of HSA were found to be altered as suggested by three-dimensional (3D) fluorescence experiments. The affinity of **1** to bind to HSA was found to be strong as indicated from its value of the binding constant (K_a = 2.89 × 10^5 M^{-1}). Intrinsic fluorescence of the protein was found to be reduced through a mechanism of static quenching as suggested from the k_q (2.01 × 10^{13} M^{-1} s^{-1}) value, the bimolecular quenching constant. The Förster resonance energy transfer (FRET) process may also be accounted for such a high k_q value. The *r* value (2.85 nm) calculated from FRET theory suggested that the distance between complex **1** (acceptor) and HSA (donor) is quite close. Complex **1** primarily bound to HSA in subdomain IIA as suggested by molecular docking studies. IC_{50} values (0.80 and 0.43 μM, respectively) obtained from the 3-(4,5-dimethylthiazol-2-yl)-2,5-diphenyltetrazolium bromide (MTT) assay with HeLa and MCF7 cells suggested remarkable in vitro anticancer activity of **1**. Nuclear dual staining assays revealed that cell death occurred via apoptosis in HeLa cells and reactive oxygen species (ROS) accumulation caused apoptosis induction. On treatment with a 5 μM dose of **1** in HeLa cells, the cell population significantly increased in the G2/M phase, while it was decreased in G0/G1 and S phases as compared to the control, clearly indicating G2/M phase arrest.

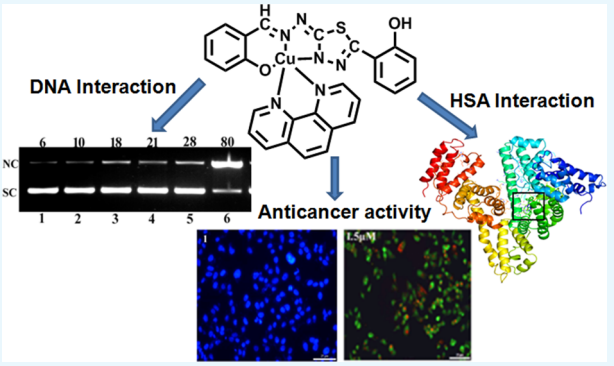

1. INTRODUCTION

The important features of chemistry and the biochemistry of copper and its role in medicine are well documented in the literature.[1] In recent years, copper complexes of Schiff base as well as other ligands[1,2] capable of binding DNA and proteins and having good cytotoxic activity toward various cancer cells are extensively studied to explore their potential to act as anticancer agents[1−31] to find suitable substitutes for widely used Pt-based anticancer metallodrugs[32−42] for treatment of various types of cancers because these drugs having limitations as they frequently show toxic effects like nephrotoxicity, ototoxicity, neurotoxicity, and development of resistance to these drugs, either acquired or inherent. Since copper is an essential trace metal ion in our body, copper(II) complexes containing suitable biologically relevant organic ligands, possessing biocompatible redox potential, and having high DNA binding propensity are expected to show good biological activities including reactive oxygen species (ROS) generation, DNA cleavage, and anticancer activity. Though a majority of these studies involved copper(II) complexes of various Schiff

Received: October 14, 2021
Accepted: December 30, 2021
Published: January 10, 2022

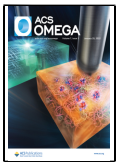

Scheme 1. Proposed Mechanism for Rearrangement of the Schiff Base and the Structure of Compound 1 Formed in This Reaction[a]

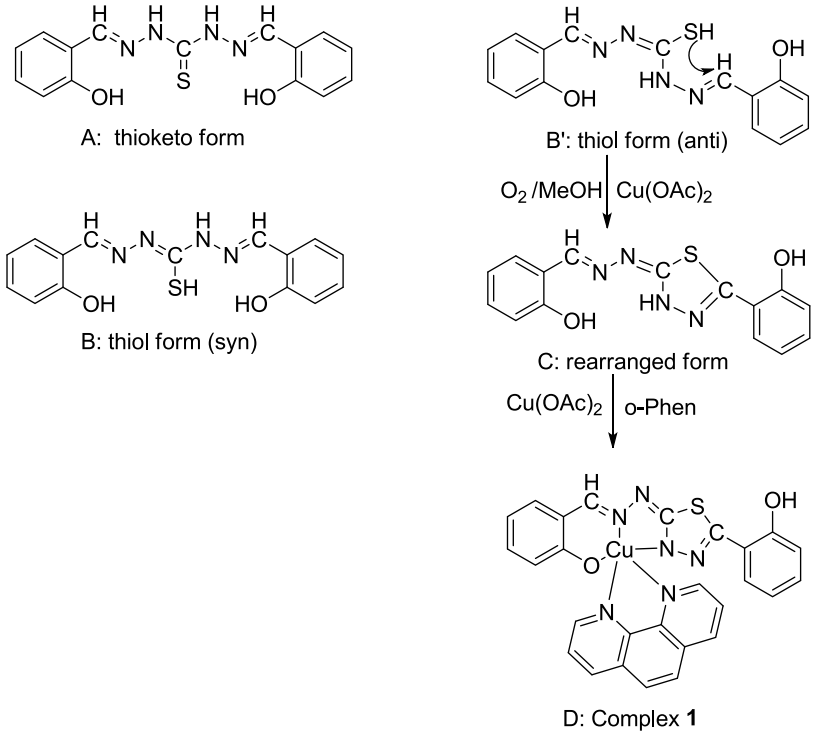

[a](A) Thioketo form, (B) thiol form (syn), (B′) thiol form (anti), and (C) rearranged form of the Schiff base and (D) complex **1**.

base ligands, there are many other ligands[5,7,18,19,23,31] that have been used to synthesize copper complexes to study their other biological properties, for example, Cu(II) complexes of salicylic acid with a superoxide dismutase mimetic property,[7] a Cu(II) complex of 2,9-bis-(2′,5′-diazahexanyl)-1,1-phenanthroline with amoebicide activity,[23] and Cu(II) complexes with mixed heterocyclic ligands having antibacterial activity[31] apart from their anticancer activity. It is noteworthy to mention specifically the copper(II) complexes with the homo- or heteroleptic heterocyclic chelating ligands that have been investigated extensively[1,2] for DNA interaction and have been found to have K_b values in the range 10^3-10^7 M^{-1}. Their structures were established by X-ray crystallography, and these complexes possessed N,N-donor polypyridyl ligands like 2,2′-bipyridine (bipy) or 1,10-phenanthroline (*o*-phen).[2] The complexes having ligands with extended planarity are found to have enhanced DNA intercalation and exhibit more cytotoxicity toward various carcinoma cells. As a result, attention was focused on synthesizing copper complexes of appropriate donor ligands along with heterocyclic planar N-donor coligands that are effective in binding and cleaving DNA and that show significant cytotoxic activity toward different cancer cell lines.[1,2,30]

It is also important to study the interaction of these complexes with serum albumin that gives an additional advantage to use them as a potential drug as it is well known that the plasma protein human serum albumin (HSA) acts as an effective carrier of many drugs.[43−52] Herein, we report a Cu(II) mononuclear compound (**1**) of a Schiff base possessing a heterocyclic ring as the major ligand formed in situ via a metal-induced[53] reaction with starting ligand 1,5-bis(salicylidene)thiocarbohydrazide.[54] This compound shows strong interaction with DNA and HSA as well as effective nuclease activity through both oxidative and hydrolytic pathways and significant cytotoxicity toward HeLa and MCF7 cells.

UV−vis absorption titration and competitive DNA binding fluorescence experiments were performed to assess interaction of **1** with CT-DNA. The DNA cleavage experiments with pUC19 supercoiled plasmid DNA revealed that complex **1** was not only capable of cleaving DNA through an oxidative pathway but also capable of cleaving DNA following the hydrolytic pathway without any external reagent. Fluorescence quenching, synchronous, three-dimensional (3D) fluorescence studies, FRET, and electronic absorbance spectroscopy were utilized to investigate the interaction of complex **1** with HSA. Cytotoxicity of complex **1** against HeLa and MCF7 cell lines was assessed using the 3-(4,5-dimethylthiazol-2-yl)-2,5-diphenyltetrazolium bromide (MTT) assay. H_2DCFDA staining revealed activation of ROS by **1**, while its apoptotic potential was studied by Hoechst and AO/PI dual staining assays. Cell cycle analysis was performed using HeLa cells.

2. RESULTS AND DISCUSSION

2.1. Synthesis and Characterization. When a methanol solution of $Cu(OAc)_2{\cdot}H_2O$ and 1,10-phenanthroline (1 mmol each) was reacted with 1,5-bis(salicylidene)-thiocarbohydrazide[54] (A, Scheme 1) in the presence of air, enolization (B) followed by cyclization[53] occurred in the Schiff base, forming in situ a new Schiff base containing a thiadiazoline ring (C, Scheme 1) that was found to coordinate to Cu^{2+} ions as an O^-NN^- chelate[53] and was stable along with a water molecule as evident from the fact that this species was detected in the ESI-MS experiment of the compound in CH_3CN with the major peak at m/z 391.02 (Figure S1A) that corresponds to $[Cu(HL)(H_2O)]^+$ or $[Cu(C_{15}H_{10}N_4O_2S)$-

https://doi.org/10.1021/acsomega.1c05750
ACS Omega 2022, 7, 2881−2896

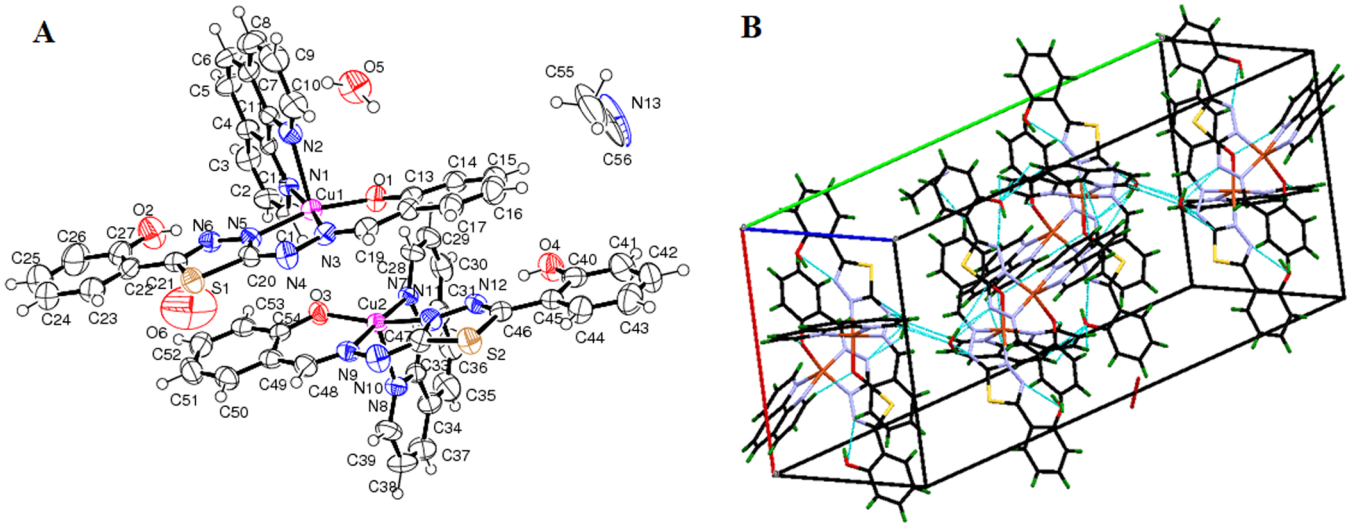

Figure 1. (A) Molecular structure of **1**. (B) Packing of the molecules in the unit cell. Important bond lengths [Å] and angles [°] for **1**: Cu(1)−O(1) 1.918(4), Cu(1)−N(5) 1.954(5), Cu(1)−N(3) 1.969(5), Cu(1)−N(1) 2.037(5), Cu(1)−N(2) 2.288(5), Cu(2)−O(3) 1.926(4), Cu(2)−N(9) 1.973(5), Cu(2)−N(11) 1.979(5), Cu(2)−N(7) 2.046(5), Cu(2)−N(8) 2.289(5), O(1)−Cu(1)−N(5) 164.7(2), O(1)−Cu(1)−N(3) 93.74(19), N(5)−Cu(1)−N(3) 79.8(2), O(1)−Cu(1)−N(1) 94.32(18), N(5)−Cu(1)−N(1) 92.33(19), N(3)−Cu(1)−N(1) 171.9(2), O(1)−Cu(1)−N(2) 98.11(19), N(5)−Cu(1)−N(2) 96.75(19), N(3)−Cu(1)−N(2) 101.30(19), N(1)−Cu(1)−N(2) 77.62(18), O(3)−Cu(2)−N(9) 92.6(2), O(3)−Cu(2)−N(11) 162.7(2), N(9)−Cu(2)−N(11) 79.7(2), O(3)−Cu(2)−N(7) 89.75(18), N(9)−Cu(2)−N(7) 177.3(2), N(11)−Cu(2)−N(7) 98.38(19), O(3)−Cu(2)−N(8) 96.28(19), N(9)−Cu(2)−N(8) 100.95(19), N(11)−Cu(2)−N(8) 100.3(2), N(7)−Cu(2)−N(8) 77.48(18).

$(H_2O)]^+$, while the peak for the protonated cyclized Schiff base (C, Scheme 1) $[H_3L + H]^+$ was observed at m/z 313.07 (Figure S1B) that corresponds to $[C_{15}H_{12}N_4O_2S + H]^+$. However, during synthesis, the fourth position is occupied by one N-donor of the bidentate *o*-phen coligand, while the other N-donor atom occupied the apical position forming a distorted square-pyramidal molecule of **1** (D, Scheme 1).

2.2. X-ray Crystal Structure. Data collection and data analyses[55−57] were performed as previously described[53] by us. Complex **1** is found to be monoclinic having space group *P*21/*c*. Two distinct molecules of **1** were found to be present in an asymmetric unit of the crystal along with half-molecule acetonitrile and $1.5H_2O$ (sesquihydrate) (Figure 1A). The Cu^{2+} ion assumes penta coordination with O^-NN^- of the cyclized Schiff base and the bidentate phenanthroline molecule, forming a slightly distorted square-pyramidal geometry. The basal plane around Cu1 is formed by O1, N3, N5, and N1 (bond lengths 1.918(4)−2.039(5) Å), and the apical position is occupied by N2 of the phenanthroline moiety (bond length 2.288(5) Å). Also, in the second copper complex, the basal plane around Cu2 is formed by O3, N9, N11, and N7 (bond lengths 1.926(4)−2.046(5) Å) and the apical position is occupied by N8 of the phenanthroline moiety (bond length 2.289(5) Å). The water molecule, H5A−O5−H5B, holds two molecules of Cu complexes through O(5)−H(5B)···N(4) ($d_{H\text{-}A}$ = 2.17(5) Å) and O(5)−H(5A)···N(10) ($d_{H\text{-}A}$ = 2.07(5) Å) intermolecular hydrogen-bonding interactions. Additionally, C−H···π and C−H···O interactions help to form the three-dimensional crystal lattice (Figure 1B).

2.3. IR and Electronic Spectra. The strong IR band at around 1620 cm^{-1} corresponding to ν(C═N) of the free Schiff base is found to be shifted to 1600 cm^{-1} when coordinated with the metal ion,[53] as seen in the IR spectrum of compound **1** (Figure S2, Supporting Information). On the other hand, a DMSO solution of this compound displayed an electronic spectrum (Figure S3A, Supporting Information) involving a crystal field transition near 610 nm, while the strong charge-transfer transitions were observed in the range of 500−270 nm. The absorbance spectrum of **1** in DMSO and that recorded for **1** in sodium phosphate buffer (20 mM) at pH 7.4 were very similar (Figure S3B, Supporting Information). It is to be noted that this compound was found to be stable in solution as revealed from the fact that no appreciable change in the absorbance was observed on standing at RT. However, fresh solutions were used to carry out all experiments.

2.4. EPR Spectra. The powder sample of compound **1** at RT and at LNT displayed strong X-band EPR spectra (Figure S4, Supporting Information), suggesting that the compound is paramagnetic. The powder spectrum shows an axial symmetry having $g_\parallel$ = 2.0403 and $g_\perp$ = 2.1030 at RT and $g_\parallel$ = 2.030 and $g_\perp$ = 2.089 at LNT. The EPR spectrum of **1** in dimethylformamide (DMF) at RT appears to be a four-line pattern (Figure S3, Supporting Information), which has resulted from the interaction of the electron with $^{63/65}$Cu nucleus, I = 3/2. Moreover, the LNT frozen glass spectrum in DMF (Figure S4, Supporting Information) is simply characteristic of a monomeric tetragonal complex ion with $g_\parallel > g_\perp$ and $A_\parallel > A_\perp$ as revealed from the analysis of the frozen glass spectrum having tetragonal character with $g_\parallel$ = 2.164, $g_\perp$ = 2.087, $A_\parallel$ = 19.08 mT, and $A_\perp \leq$ 4 mT.

2.5. Cyclic Voltammetry. The redox property of **1** was studied in DMF at RT in a dinitrogen atmosphere in the presence of 0.1 M $[N(n\text{-}Bu)_4]ClO_4$ as the supporting electrolyte using cyclic voltammetry (Figure S5, Supporting Information). No well-defined reduction peak is observed except a weak and broad reductive response at −1.16 V, for an initial negative scan starting from 0.0 V. Scan reversal showed broad oxidative responses at +0.46 and +1.54 V, and further reversal of this scan showed a reductive response near +0.12 V. However, for the oxidative response at +1.54 V, no associated reduction wave was noticed, indicating an irreversible process,

https://doi.org/10.1021/acsomega.1c05750
ACS Omega 2022, 7, 2881−2896

possibly involving ligand center oxidation at this potential. The reduction wave near +0.12 V was coupled to a broad oxidative peak near +0.46 V, most likely due to the Cu(II)/Cu(I) redox couple with a ΔE_p = 340 mV, suggesting a quasi-reversible process.

2.6. CT-DNA Binding. *2.6.1. UV−Vis Spectroscopic Analysis.* Electronic spectroscopy was used to study the affinity of complex **1** for binding to CT-DNA. Electronic spectra of **1** recorded in the absence and presence of CT-DNA are illustrated in Figure 2. As the concentration of CT-DNA

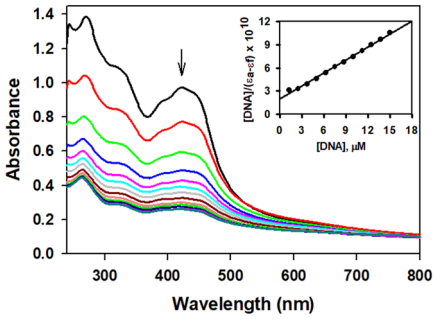

Figure 2. Electronic spectrum changes for **1** [5×10^{-5} M] after titrating with CT-DNA (0−15 μM) in Tris−HCl (10 mM) at pH 7.45. The decrease in absorbance with an increasing amount of CT-DNA is shown with the arrow. The [DNA]/($\varepsilon_a - \varepsilon_f$) versus [DNA] linear plot is shown in the inset.

was increased, the spectral bands of the complex got affected, showing a significant reduction in absorbance. The observed hypochromism suggested intercalative binding and had resulted owing to strong stacking between aromatic groups and base pairs of CT-DNA. The K_b of complex **1** with CT-DNA was determined using the Wolfe−Shimer equation (eq 1)[58] by plotting [DNA]/($\varepsilon_a - \varepsilon_f$) versus [DNA].

$$\frac{[\mathrm{DNA}]}{(\varepsilon_a - \varepsilon_f)} = \frac{[\mathrm{DNA}]}{(\varepsilon_b - \varepsilon_f)} + \frac{1}{K_b(\varepsilon_b - \varepsilon_f)} \quad (1)$$

where [DNA] represents the CT-DNA concentration used and the apparent, free, and bound metal complex extinction coefficients are represented by ε_a, ε_f, and ε_b, respectively.

The classical intercalator ethidium bromide was reported to have an intrinsic binding constant (K_b) value of 1.40×10^5 M^{-1} in Tris−HCl buffer (25 mM) at pH 7.33.[59] The K_b for **1** under study was determined to be 2.85×10^5 M^{-1}, suggesting that it has high affinity for DNA binding.

2.6.2. Competitive DNA Binding by Fluorescence Studies. The planar nonemissive dye ethidium bromide (EB) upon binding to DNA intercalatively emits intense fluorescence that can then be quenched by adding another molecule capable of binding DNA intercalatively by displacing DNA-bound EB, forming a nonemissive DNA complex, and the amount of fluorescence quenching of the EB-bound DNA is utilized to measure the affinity of the added molecule to DNA.[60] When complex **1** was added in incremental amounts to the EB-bound CT-DNA solution, the emission intensity decreased (as shown in Figure 3) due to the gradual displacement of DNA-bound EB by the complex. The quenching of EB-bound DNA by **1** was found to be in good agreement with the linear Stern−Volmer equation (eq 2) as revealed from the linear plot of F_0/F versus [complex], depicted in the inset of Figure 3.

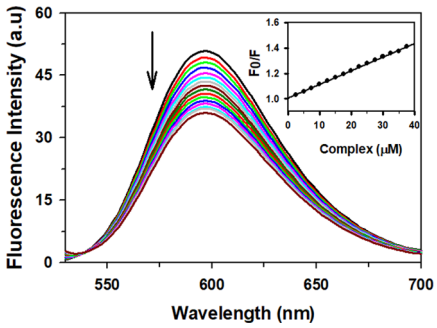

Figure 3. Competitive DNA binding by fluorescence studies for the EB displacement assay for **1**. Emission spectra of CT-DNA (50 μM) and EB (2 μM) in Tris−HCl buffer (10 mM) at pH = 8.0 in the absence of **1** (top black curve) and in the presence of different concentrations of **1**, λ_{ex} = 510 nm. The arrow shows a decrease in intensity with an increase in the concentration of **1**. The linear plot of F_0/F versus [complex] is depicted in the inset.

$$\frac{F_0}{F} = 1 + K_{SV}[Q] \quad (2)$$

where F_0 is the fluorescence intensity of the DNA-EB adduct in the absence and F is the fluorescence intensity in the presence of the complex (quencher). [Q] is the quencher concentration, and K_{SV} is the Stern−Volmer quenching constant.

K_{app} (the apparent binding constant) for **1** was estimated using eq 3.

$$K_{EB} \times [\mathrm{EB}] = K_{app} \times [\mathrm{complex}]_{50} \quad (3)$$

where $[\mathrm{complex}]_{50}$ represents the concentration of the complex at which the fluorescence intensity of the DNA-EB adduct is reduced to 50% and $K_{EB} = 1.0 \times 10^7$ M^{-1}.[61]

The value of K_{SV} obtained from the slope of the F_0/F vs [Q] plot was found to be 1.07×10^4 M^{-1} (R^2 =0.99906 for 15 points), suggesting strong affinity of **1** for CT-DNA. The K_{app} value for **1** was estimated as 1.3×10^6 M^{-1}. Other reported copper(II) complexes have similar values for K_{app}.[62] The closeness in the K_{app} value of complex **1** to that of ethidium bromide ($K_{EB} = 1 \times 10^7$ M^{-1}) indicates that **1** is comparable to classical intercalator EB.

2.6.3. pUC19 DNA Cleavage Activity. The cleavage of pUC19 plasmid DNA promoted by **1** was investigated by gel electrophoresis. It is known that pUC19 plasmid DNA exists in a compact supercoiled conformation (form I). The supercoiled form (SC) of DNA is converted to nicked circular (NC) form (form II) when there is single-strand scission of supercoiled DNA, while it is converted to the linear form (form III) in the case of double-strand scission. In gel electrophoresis, form I usually migrates faster toward the anode than form II and the migration rate of form III is between those of form I and form II.[63] DNA cleavage proceeds via two major pathways, namely, an oxidative pathway targeting the base and/or sugar and a hydrolytic pathway involving the hydrolysis of phosphodiester linkages.[64] Figures 4 and 5 illustrate gel electrophoretic separation showing the cleavage of pUC19 DNA induced by complex **1** in both oxidative and hydrolytic conditions, respectively.

Oxidative DNA cleavage (Figure 4) was performed by treating supercoiled pUC19 DNA with different concentrations of **1** (0−10 μM) in the presence of H_2O_2. As seen from Figure 4, the intensity of the band pertaining to SC DNA (form I) decreases, while that of the nicked circular (form II)

https://doi.org/10.1021/acsomega.1c05750
ACS Omega 2022, 7, 2881−2896

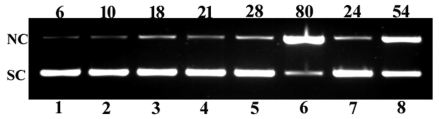

Figure 4. Cleavage of pUC19 DNA (200 ng) in Tris−HCl buffer (50 mM) at a pH 8.0 through the oxidative pathway at 37 °C. (a) Lane 1, DNA + H_2O_2 (1 mM) control; lane 2, DNA + **1** (0.5 μM) + H_2O_2 (1 mM); lane 3, DNA + **1** (1 μM) + H_2O_2 (1 mM); lane 4, DNA + **1** (2.5 μM) + H_2O_2 (1 mM); lane 5, DNA + **1** (5 μM) + H_2O_2 (1 mM); lane 6, DNA + **1** (10 μM) + H_2O_2 (1 mM); lane 7, DNA + **1** (10 μM) + H_2O_2 (1 mM) + DMSO (2 μL); lane 8; DNA + **1** (10 μM) + H_2O_2 (1 mM) + NaN_3 (500 μM).

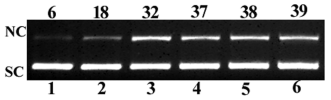

Figure 5. Cleavage of pUC19 DNA (200 ng) in Tris−HCl buffer (50 mM) at a pH 8.0 through the hydrolytic pathway at 37 °C. (a) Lane 1, only pUC19 DNA as the control; lane 2, pUC19 DNA + **1** (50 μM); lane 3, pUC19 DNA + **1** (100 μM); lane 4, pUC19 DNA + **1** (150 μM); lane 5, pUC19 DNA + **1** (200 μM); lane 6, pUC19 DNA + **1** (250 μM).

form increases, as seen in lanes 1−6. The cleavage efficiency was estimated from the ability of **1** to transform SC DNA to the nicked open circular form. Surprisingly at 10 μM, complex **1** is capable of converting 80% of SC to the NC form (Figure 4, lane 6), suggesting that **1** is highly efficient in cleaving DNA in the presence of an oxidant. To assess the role of radicals in DNA damage, reactions were carried out by incubating complex **1** with DNA in the presence of hydroxyl radical scavenger DMSO (Figure 4, lane 7) and singlet oxygen scavenger NaN_3 (Figure 4, lane 8). The results showed that DNA cleavage by **1** was considerably inhibited in the presence of both of these classical radical scavengers; however, the extent of inhibition was much more pronounced in the presence of DMSO, thus pointing that mainly hydroxyl radicals ($OH^{\bullet}$) are responsible for oxidative DNA cleavage shown by **1**. To be precise, Cu(I) species that is produced from the reduction of Cu(II) ions by superoxide anions ($O_2^{\bullet-}$) can reduce H_2O_2 to hydroxyl radicals ($OH^{\bullet}$), which is considered to be the main species responsible for damaging DNA in oxidatively stressed cells.[65]

$$Cu^{2+} + O_2^{\bullet-} \rightarrow Cu^{+} + O_2$$

$$Cu^{+} + H_2O_2 \rightarrow OH^{\bullet} + Cu^{2+}$$

Attempts were also made to see whether **1** was capable of cleaving DNA via hydrolysis involving the phosphodiester bonds. As no external chemical reagents or light is involved in hydrolytic cleavage, it has high biological significance.[66] Experiments were done using supercoiled pUC19 DNA treated with different concentrations of **1** (0−250 μM) in the dark without adding any external agent (Figure 5). Although not much, **1** was capable of rupturing DNA to some extent without the presence of any coreagent, as seen in Figure 5.

From the above studies, it may be concluded that **1** is more efficient in oxidative DNA cleavage. The results also indicate the involvement of $OH^{\bullet}$ as the dominant species in the cleavage pathway, possibly through oxidation of deoxyribose it brings about DNA cleavage.

2.7. Interaction Studies with HSA. *2.7.1. Fluorescence Quenching.* HSA in blood plasma is capable of reversibly binding metallodrugs and is selectively accumulated in tumor tissues, which enables selective delivery of drugs to target sites, and thus, interaction studies with HSA are regarded vital in the development of anticancer agents.[46−49] HSA contains three structurally similar domains (I, II, III), each of which is composed of two subdomains, denoted IA, IB; IIA, IIB; and IIIA, IIIB. Each subdomain has a main cavity for interaction with ligands. HSA fluorescence is primarily owing to amino acid residue tryptophan (Trp), which is present in subdomain IIA, and it is seldom exploited for interaction studies of HSA with other molecules through fluorescence spectroscopy;[67,68] for example, interaction with a drug molecule can alter the fluorescence spectra of HSA and the extent of this effect will depend on the concentration and the average distance between the molecule and the tryptophan residue.

In our study, HSA interaction with complex **1** was followed by recording the HSA fluorescence spectrum with increased amounts of **1**, after exciting at 295 nm (Figure 6), so that the emission fluorescence is restricted to tryptophan.[67] The characteristic broad band at around 345 nm resulting from fluorescence emission of HSA was found to be quenched significantly as the complex **1** concentration was increased, suggesting strong interaction between **1** and HSA. A slightly

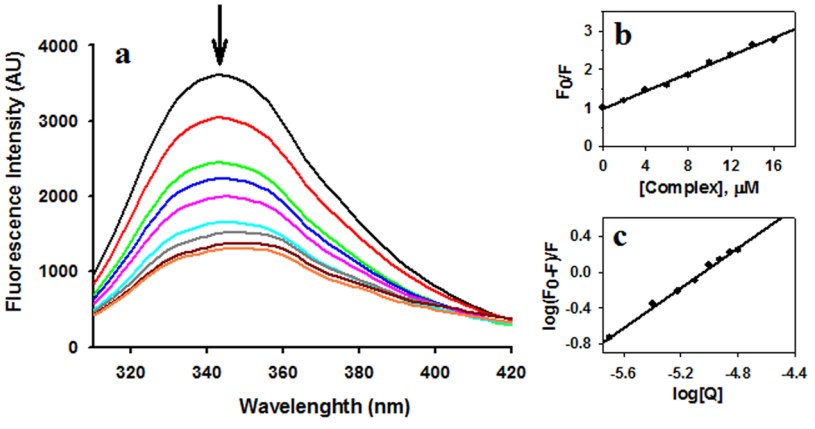

Figure 6. (a) Fluorescence spectra of HSA (4 μM; λ_{exi} = 295 nm) in the absence (top black curve) and presence of increasing amounts of complex **1**. The arrow shows the quenching of fluorescence on addition of increased concentrations of **1**. (b) Stern−Volmer plot and (c) modified Stern−Volmer plot of complex **1** with HSA.

https://doi.org/10.1021/acsomega.1c05750
ACS Omega 2022, 7, 2881−2896

lower energy shift in the spectra was observed; this bathochromic shift suggests perturbation of the microenvironment around tryptophan residue and that this residue has a less hydrophobic environment. The fluorescence intensity data was analyzed, and the Stern−Volmer plot of F_0/F versus [Q] (Figure 6b) revealed good linearity. The parameters from quenching experiments were determined using the Stern−Volmer equation (eq 4) and the modified Stern−Volmer equation (eq 5).

$$\frac{F_0}{F} = 1 + K_{SV}[Q] = 1 + k_q\tau_0[Q] \quad (4)$$

where F_0 is the HSA fluorescence intensity in the absence of **1**, F is the HSA fluorescence intensity in the presence of **1**, K_{SV} is the Stern−Volmer constant, [Q] is the molar concentration of complex **1** (quencher), k_q is the bimolecular quenching rate constant, and τ_0 is the average lifetime of HSA fluorescence in the absence of the quencher.

$$\log\frac{(F_0 - F)}{F} = \log K_a + n\log[Q] \quad (5)$$

where K_a is the binding constant and n is the number of binding sites.

The bimolecular quenching constant k_q was estimated from eq 6, wherein the τ_0 of HSA was taken as 5.71×10^{-9} s.[69]

$$k_q = \frac{K_{SV}}{\tau_0} \quad (6)$$

The binding constants and relevant parameters determined from Stern−Volmer (S−V) and modified Stern−Volmer (modified S−V) plots are given in Table 1.

The K_{SV} value obtained from the slope of the Stern−Volmer plot was $\sim 10^5$ M^{-1}, suggesting that strong quenching is exhibited by complex **1**. The bimolecular quenching constant k_q was calculated using eq 6, and the k_q value was of the order of 10^{13} M^{-1} s^{-1}. The considerably high k_q value ($>10^{11}$ M^{-1} s^{-1}) was probably an indication of static quenching.[69,71]

The fluorescence data was further examined using the modified Stern−Volmer equation (eq 5), and the binding constant (K_a) and binding stoichiometry (n) of the complex **1**/HSA system were thereby determined. Figure 6c illustrates the linear dependence of $\log(F_0 - F)/F$ on $\log Q$ for complex **1**. The number of binding sites (n) in HSA for the molecule was obtained from the slope of the modified Stern−Volmer plot, while its intercept ($\log K_a$) gave an idea about the binding constant.[69,70] The value of n was close to 1 for the HSA−complex **1** system, which implies that complex **1** occupies only a single binding site in HSA. The binding constant K_a of magnitude 10^5 M^{-1} indicates strong binding of **1** with HSA. The value of the binding constant K_a was used to determine the free energy change, ΔG of binding of complex **1** to HSA, by eq 7.[70]

$$\Delta G = -RT\ln K_a \quad (7)$$

The negative free energy change (Table 1) indicates that the interaction of **1** with HSA is favorable from the thermodynamic aspect.

2.7.2. Synchronous Fluorescence Spectroscopy. Synchronous fluorescence spectroscopy is a useful tool that is often used to study the microenvironmental changes of macromolecules and thus has been widely used to investigate the influence of ligands on HSA conformation.[48,67,72] A blue shift

Table 1. Fluorescence Quenching Results: Parameters Obtained from S−V and Modified S−V Plots for Quenching of HSA Fluorescence by Complex 1

complex	SV equation	R^2	$K_{SV} \times 10^5$ (M^{-1})	$k_q \times 10^{13}$ M^{-1} s^{-1}	modified SV $\log(F_0 - F)/F = \log K_a + n\log[Q]$	binding constant $K_a \times 10^5$ (M^{-1}))	R^2	no. of binding sites (n)	free energy ΔG (kJ mol^{-1})
1	$Y = 115\,300.16X + 0.970$	0.992	1.15	2.01	$Y = 1.08X + 5.461$	2.89	0.989	1.08	−31.16

https://doi.org/10.1021/acsomega.1c05750
ACS Omega 2022, 7, 2881−2896

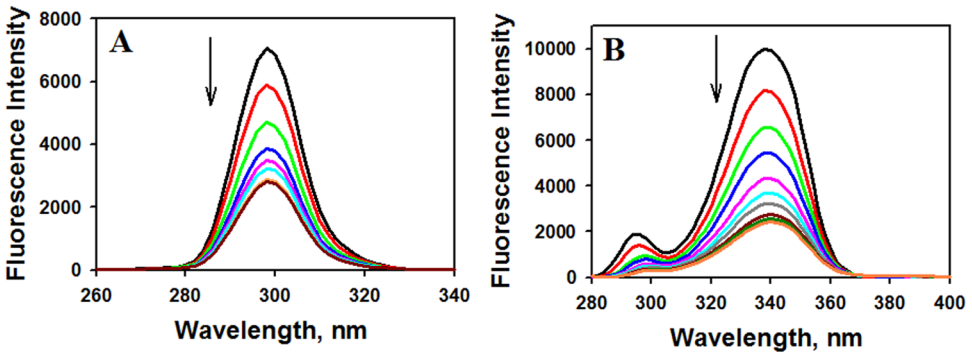

Figure 7. Synchronous spectra of HSA (4 μM) in sodium phosphate buffer (20 mM) at pH 7.4 before and after addition of (A) complex **1** (0−14 μM), $\Delta\lambda$= 15 nm and (B) complex **1** (0−18 μM), $\Delta\lambda$ = 60 nm.

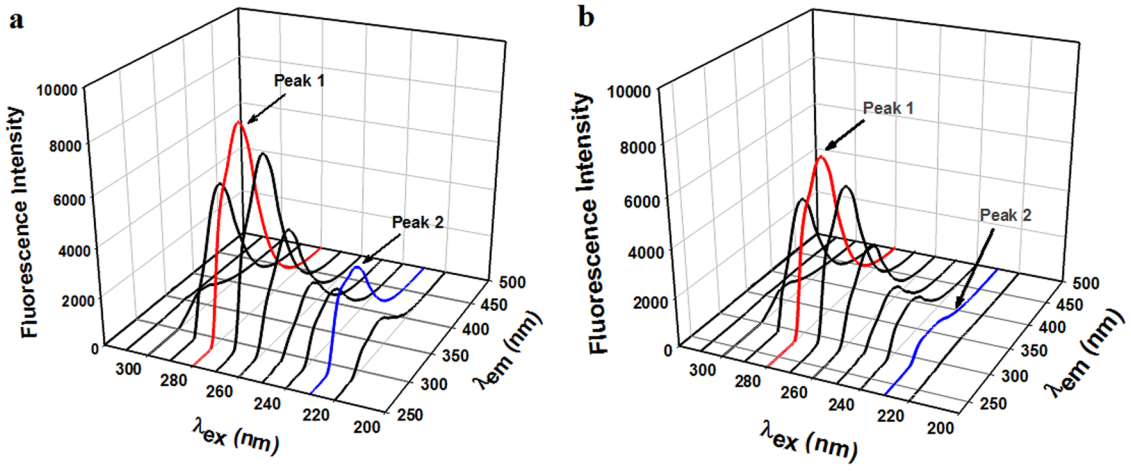

Figure 8. 3D fluorescence spectra of (a) HSA and (b) HSA + **1** (1:1).

Table 2. Results of 3D Fluorescence Experiments

	peak 1			peak 2		
	peak position ($\lambda_{ex}/\lambda_{em}$)	fluorescence intensity (AU)	$\Delta\lambda$ (nm)	peak position ($\lambda_{ex}/\lambda_{em}$)	fluorescence intensity (AU)	$\Delta\lambda$ (nm)
HSA	280/336	8052	56	230/332	3287	102
HSA + **1** (1:1)	280/336	6576	56	230/316	627	86

in the spectra suggests a hydrophobic environment for the amino acid residues; on the other hand, a lower energy shift suggests a polar environment for amino acid residues. At $\Delta\lambda$ = 15 nm, fluorescence spectra of the synchronous experiment provide information of the microenvironment around the tyrosine residue (Tyr), while at $\Delta\lambda$ = 60 nm, it provides the information of the microenvironment around the tryptophan residue (Trp)[48,67,72] ($\Delta\lambda = \lambda_{em} - \lambda_{ex}$). As seen from the synchronous fluorescence spectra with HSA (Figure 7) at $\Delta\lambda$ = 15 nm, the intensity was 7052 au at 298 nm, which on addition of complex **1** was reduced by 60.2% to 2807 au but without any shift in wavelength maxima. On the other hand, at $\Delta\lambda$ = 60 nm, the intensity was 9998 au at 338 nm, and on addition of complex **1**, it was quenched even more, by 75.8% to 2423 au accompanied by a 2 nm shift toward a longer wavelength. The steady reduction in the intensity of fluorescence observed upon addition of increasing amounts of **1** at both $\Delta\lambda$ = 15 nm and $\Delta\lambda$ = 60 nm suggested that **1** binds to HSA in the hydrophobic cavity in the vicinity of Tyr and Trp residues. Also, at $\Delta\lambda$ = 60 nm, the maximum of the emission peak was shifted from 338 to 340 nm, which indicated that mainly the microenvironment around the tryptophan residue was disturbed.

2.7.3. 3D Fluorescence Spectroscopy. 3D fluorescence spectroscopy provides information about conformational changes in proteins upon binding of metal complexes.[46,61,71] Figure 8 shows the 3D fluorescence spectra of HSA with and without complex **1**, and the results are summarized in Table 2. As observed in Figure 8, peak 1 was moderately quenched by 18.3%, indicating that **1** on binding induced certain conformational changes in HSA, possibly by perturbing the hydrophobic microenvironment near tryptophan (Trp) and tyrosine (Tyr) residues. Also, it was noted that peak 2 was drastically quenched by 81% and associated with a considerable shift of 16 nm toward a shorter wavelength; this implied that this interaction may have altered the peptide backbone configuration as well.

2.7.4. Conformation Investigation Using UV−Vis Spectroscopy. Static and dynamic quenching are the two common methods for fluorescence quenching and are differentiated by their differing perturbation effect on the absorption spectrum of the fluorophore. It is reported that there is no change in the absorption spectrum of fluorophores in the case of dynamic quenching; on the other hand, static quenching does have an influence on the fluorophore spectrum.[48,73] To gain insight

https://doi.org/10.1021/acsomega.1c05750
ACS Omega 2022, 7, 2881−2896

into the method involved in quenching of the fluorescence of HSA by **1**, the UV−visible spectrum of HSA was recorded at RT (25 °C) and the effect of complex **1** on the absorption spectrum was studied. From Figure S6, it was observed that upon addition of complex **1**, the absorbance at 216 nm was significantly decreased accompanied by a bathochromic shift of 17 nm, which strongly supports static quenching and indicates an alteration in the protein secondary structure. Also, it was observed that the intensity of the 280 nm peak, which is associated with the $\pi \rightarrow \pi^*$ transition of Trp, Tyr, and Phe, is slightly increased, suggesting alteration of the microenvironment around these amino acids.[69]

2.7.5. Energy-Transfer and Binding Distance Using FRET. Fluorescence resonance energy transfer (FRET) occurs when radiationless energy transfer takes place from an excited donor to a suitable acceptor. FRET is a distance-dependent photophysical process and therefore can be appropriately used to determine the separation distance between the donor (fluorophore) and the acceptor. According to the Förster theory, the efficiency of energy transfer (E) is related to the distance between the donor and accepter (r), and the critical energy-transfer distance also known as Förster's radius (R_0) is determined according to the relation given in eq 8.[67,74]

$$E = \frac{R_0^6}{R_0^6 + r^6} = 1 - \frac{F}{F_0} \tag{8}$$

where F_0 is the fluorescence intensity of the donor in the absence and F is the fluorescence intensity of the donor in the presence of the acceptor. The critical distance R_0, where the efficiency of energy transfer is 50%, is a function of the spatial orientation factor (K^2), the quantum yield of fluorescence of the donor (ϕ_D), the refractive index of the medium (n), and the extent of overlap (J) between the donor emission spectrum and acceptor absorption spectrum (Figure 9) and is expressed as given below in eq 9.[67]

$$R_0 = 0.02108(K^2 \phi_D n^{-4} J)^{1/6} \tag{9}$$

For the conditions used in our experiment, values of K^2, ϕ_D, and n were considered as 2/3, 0.118, and 1.33, respectively,[69,75] and J, which is the overlap integral, was calculated using eq 10.[76]

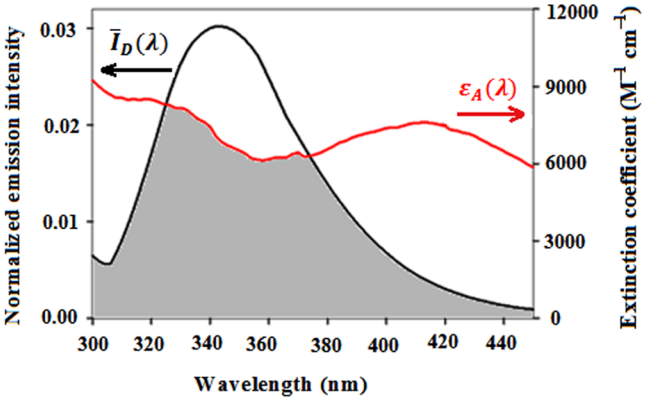

Figure 9. Extent of overlap (shaded gray) between the normalized fluorescence spectrum of the 4 μM HSA donor (left) and the absorption (ε) spectrum of (4 μM) acceptor complex **1** (right).

$$J = \int \bar{I}_D(\lambda)\varepsilon_A(\lambda)\lambda^4 \, d\lambda \tag{10}$$

where $\bar{I}_D(\lambda)$ denotes the normalized donor fluorescence emission and $\varepsilon_A(\lambda)$ represents the molar extinction coefficient of the acceptor at wavelength λ.

Calculations were done using eqs 8−10 above, and the results are tabulated in Table 3. The value of r = 2.85 nm

Table 3. FRET Results of HSA−Complex Interactions

compound	E	$J \times 10^{14}$ (nm^4 M^{-1} cm^{-1})	R_0 (nm)	r (nm)
1	0.32	1.15	2.52	2.85

indicates that the donor and acceptor are very much close to each other and hence strong binding interaction can be expected between them. Moreover, the value of r is less than 8 nm and follows $0.5R_0 < r < 1.5R_0$, thereby indicating that the quenching of HSA fluorescence might have been due to complex formation between HSA and metal complex **1**, and this further supports the static quenching mechanism.[77]

2.8. Molecular Docking of Complex 1 with HSA. To understand the binding interactions of proteins and small molecules at the atomistic level, the molecular docking method is considered to be one of the very important techniques in drug design.[46−48] We have performed docking experiments with HSA to assess the potential interaction site of **1** in HSA. The 3D structure of crystalline HSA reveals that it is composed of three major domains, namely I, II, and III. Domain I is composed of amino acid residues 1−195, domain II includes amino acid residues 196−383, and domain III involves amino acid residues 384−585.[77] Each domain is further subdivided into two subdomains (A and B). The two primary ligand-binding cavities are located in subdomains IIA and IIIA, which are known as Sudlow's sites I and II, respectively. Apart from these, another binding site is located in subdomain IB. It is to be noted that prime residue Trp214 is situated in site I, neighboring with Lys195, Lys199, Arg218, and Arg222.[78,79] Docking was performed to understand the binding affinity between complex **1** and HSA (PDB ID: 1H9Z), which is the most abundant carrier protein in the blood. The optimal binding conformations of **1**-HSA are shown in Figure 10. The lowest binding energy obtained from the docking simulation is −11.2 kcal/mol. The binding energy for iterations in each run ranges between −8.5 kcal/mol and −11.2 kcal/mol. The intermolecular hydrogen bonds are presented in Table 4 along with the corresponding bond lengths. The data (Table 4) indicates that there are three strong hydrogen bonds with Arg222 and one with Lys199. It is worth pointing out that both these amino acids are located at the site I entrance, which explains the reason behind the fluorescence quenching of Trp214 in the presence of complex **1**. In addition, there is also a hydrogen bond with Glu153. Therefore, from the above docking studies, we may conclude that there is good binding between complex **1** and HSA. The complex partly enters subdomain 1B, although the interaction occurs mainly in subdomain IIA.

2.9. Anticancer Activity. *2.9.1. Cytotoxic Activity Using the MTT Assay.* In vitro anticancer activity of complex **1** was tested against two cancerous cell lines, namely, human cervical cancer HeLa and human breast cancer MCF7, and the cytotoxic activity was tested for one noncancerous HaCaT human cells by the MTT assay with respect to standard anticancer drug cisplatin. The cell viability was found to

https://doi.org/10.1021/acsomega.1c05750
ACS Omega 2022, 7, 2881−2896

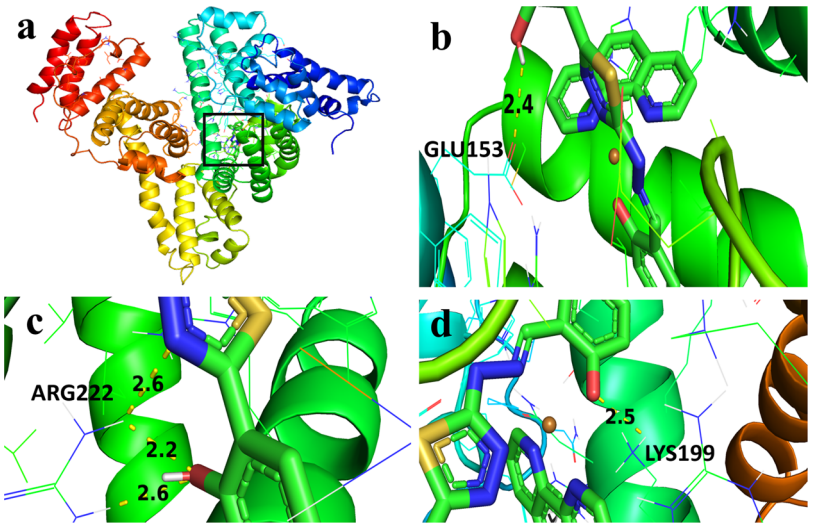

Figure 10. Docking of complex **1** with HSA. (a) Full view of complex **1** in HSA, (b) detailed illustration of interaction of complex **1** with Glu153 (subdomain IB), (c) detailed illustration of interaction of complex **1** with Arg222 (subdomain IIA), and (d) detailed illustration of interaction of complex **1** with Lys199 (subdomain IIA). H-bonds are shown in yellow dashed lines, and the involved amino acids are labeled. For clarity, the remaining portions of the protein structure are hidden.

Table 4. Molecular Docking Analysis for Formation of H-Bonds between 1 and HSA (HSA: 1H9Z)[a]

binding site	complex **1** atom	HSA atom	distance (Å)
site I	O2	HE atom of ARG222	2.6
	N6	1HH2 atom of ARG222	2.6
	O2	1HH2 atom of ARG222	2.2
	H2A	OE1 atom of GLU153	2.4
	O1	HZ3 atom of LYS199	2.5

[a]Crystal structure of **1** with labeled atoms shown in Figure 1A is used in this analysis.

Table 5. IC_{50} Values Obtained for Complex 1 and Cisplatin from Their MTT Assay Using HeLa and MCF7 Cells

	IC_{50} values[a] (μM)	
compound	HeLa	MCF7
1	0.8047 ± 0.1378	0.4390 ± 0.1139
cisplatin	31.24 ± 1.38	99.6481 ± 0.051

[a]IC_{50} values are the mean concentrations of drugs to inhibit 50% of cancer cells (in μM). An average of three replicates is taken and presented as mean ± SD.

decrease as the concentration of **1** was increased (Figure 11), showing that the anticancer potency of complex **1** was dose-dependent. The IC_{50} values (Table 5) revealed that complex **1** is highly toxic against HeLa and MCF7 cancer cells and comparatively less toxic to HaCaT normal cells (Figure S7, Supporting Information). Additionally, along with compound **1**, the activity of cisplatin, which is known to be one of the most clinically successful drugs, was also tested in HeLa and MCF7 cell lines under the same experimental conditions (Figure S8, Supporting Information). As observed (Figure 11, Table 5), complex **1** showed significantly higher anticancer activity as compared to cisplatin in both the cell lines tested. It is to be noted here that cell viability studies using cisplatin with HeLa and MCF7 cells have been reported for different experimental conditions.[80−84]

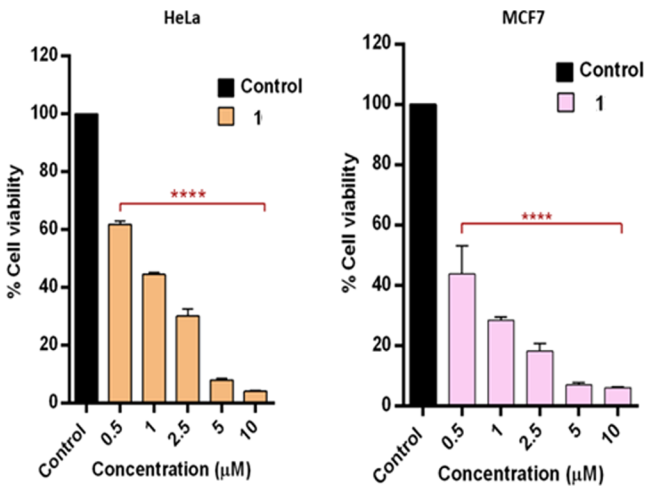

Figure 11. Cell viability results from the MTT assay for HeLa and MCF7 cancer cells with **1** for 24 h. Statistical analysis was performed with GraphPad Prism. **** indicates a significant (p < 0.0001) decrease in cell viability as compared to the control.

2.9.2. Nuclear Staining Using Hoechst 33342. Figure 12 shows the changes in morphology that were instigated by **1** in HeLa cells. To monitor these morphological changes, fluorescence microscopy was performed on both untreated and complex-treated HeLa cells stained with Hoechst 33342. It is evident from Figure 12 that the control cells were found to be stained uniformly blue. The treated cells exhibited specific features of apoptosis-like fragmented nuclei, bright staining, and condensed chromatin. These findings further support that **1** is efficient in bringing about apoptosis in HeLa cells.

2.9.3. Acridine Orange/Propidium Iodide (AO/PI) Double Staining. AO/PI staining is performed to distinguish among live, dead, and the different stages of dying cells using fluorescence microscopy. AO permeates both live and dead cells and fluoresces green. PI enters only dead cells, emitting red fluorescence. However, when both AO and PI are used together, all live nucleated cells fluoresce green and all dead nucleated cells fluoresce red, owing to Förster resonance energy transfer (FRET).[85,86] The experimental results showed

https://doi.org/10.1021/acsomega.1c05750
ACS Omega 2022, 7, 2881−2896

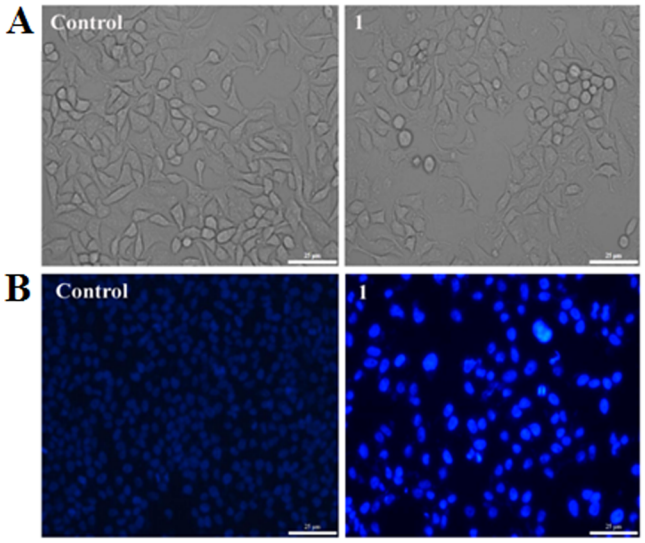

Figure 12. Morphological changes in HeLa cells after treatment with **1**. (A) Bright-field images and (B) blue fluorescent images stained with Hoechst 33342 with 20× magnification. Scale bar: 25 μm.

(Figure S9) that the live cells having intact nuclei used as control displayed green fluorescence. However, the cells treated with increased concentrations of complex **1** showed morphological changes. The cells that were in the early apoptotic stage emitted orange-green fluorescence, and the cells that have reached late apoptosis exhibited orange-red fluorescing nuclei, owing to PI binding with denatured DNA. These findings further confirm that complex **1** induces apoptosis in HeLa cells.

2.9.4. Estimation of ROS by the H_2DCFDA Assay. Several studies have shown that the cytotoxic activity of copper(II) complexes can be mediated by ROS generation.[87−89] Copper being redox-active is capable of changing its oxidation state using physiological conditions inside cells, and this redox property is liable for catalytic activity and potential toxicity of this metal. Cu(II) is readily reduced to Cu(I) upon interaction with biological molecules, and the resulting Cu(I) species on reacting with O_2 yields $O_2^{\bullet-}$, which is responsible for generating other ROS.

To investigate whether complex **1** has the ability to induce changes in intracellular ROS levels, the 2′,7′-dichlorodihydrofluorescein diacetate (H_2DCFDA) assay was conducted. The fluorogenic cell-permeant dye H_2DCFDA was used to detect ROS within the cells. To evaluate the role of ROS production in the toxic behavior of complex **1**, HeLa cells were treated with different doses of **1** and stained with H_2DCFDA. After entering the cells, H_2DCFDA was transformed to nonfluorescent H_2DCF due to deacetylation by cellular esterases. H_2DCF underwent ROS-mediated oxidation to 2′,7′-dichlorofluorescein (DCF), which exhibits green fluorescence[53,88] and is detected by fluorescence spectroscopy. Emission was measured at 530 nm after excitation at 485 nm. In this experiment, *tert*-butyl hydrogen peroxide (*t*-BHP) capable of damaging macromolecules like DNA and lipids, which leads to oxidative stress in cells that in turn triggers ROS generation, was used as the positive control. Moreover, *t*-BHP produced more stable radical species and was therefore preferred over H_2O_2 as a positive control in oxidative stress-related studies.[89] As seen in Figure S10, ROS formation increased along with increasing complex **1** concentration as detected by the intense green fluorescence intensity compared to the control comprising untreated cells. These observations further supported the results seen in oxidative DNA cleavage experiments. These findings unanimously suggested that ROS generation is escalated and oxidative stress is involved in the process of complex **1** cytotoxicity.

2.9.5. Cell Cycle Analysis. To explain cell growth inhibition by complex **1**, we studied the effect of complex **1** (0−5 μM) on cell cycle distribution in HeLa cells using flow cytometry. The DNA flow cytometric analysis (Figure S11) indicated that with treatment of 1.5 and 2.5 μM doses of complex **1** for 24 h, G0/G1 phase arrest of the cell cycle was induced. While upon treatment with a 5 μM dose, the population of cells significantly increased in the G2/M phase, while the cell population was found to decrease in G0/G1 and S phases, clearly pointing to the arrest of the G2/M phase. It should be pointed out in this context that, although a considerable effect on the inhibition of HeLa cell growth was seen from the MTT assay at a 0.5 μM dose of complex **1** (Figure S11), this dose of complex **1** did not show any specific phase arrest of the cell cycle; thus, possibly at this dose, **1** induces nonspecific arrests at all of the phases of the cell cycle. Similar observations have been reported by Han et al.[90]

3. CONCLUSIONS

A mononuclear complex (**1**) of copper(II) with a Schiff base ligand containing a heterocyclic thiadiazoline ring was isolated and characterized by physicochemical methods, and its molecular structure was confirmed by single-crystal X-ray crystallography. UV−vis spectroscopic studies suggested that the compound intercalatively binds to CT-DNA, and this was further supported by an ethidium bromide displacement experiment performed using fluorescence spectroscopy. Strong oxidative and moderate hydrolytic cleavage of SC pUC19 DNA was observed in the presence of this compound. Significant cytotoxicity of this compound was observed in HeLa and MCF7 cancer cells as revealed from the MTT assay, while it exhibited relatively low toxicity toward normal HaCaT cells as reflected from their IC_{50} values. Nuclear staining assays revealed cell death prompted by this compound in HeLa cells via an apoptotic pathway. ROS generation in HeLa cells in the presence of compound **1** suggested that it is an activator of ROS in this cell line. A quenching experiment using fluorescence spectroscopy showed that this compound interacts strongly with HSA. Synchronous and 3D fluorescence experiments suggested that interaction of **1** with HSA resulted in microenvironmental changes altering the HSA conformation, and this was augmented by the results obtained from absorption spectroscopic experiments performed with HSA in the absence and presence of the compound. The *r* value (2.85 nm) calculated from FRET suggested that HSA (donor) and complex **1** (the acceptor) exhibited quite close interaction. The molecular docking study suggested that subdomains IIA and IB of HSA are the preferred binding sites for **1**.

4. MATERIALS AND METHODS

4.1. Materials. Thiocarbohydrazide and salicylaldehyde were obtained from Aldrich. Cisplatin was purchased from Sigma-Aldrich. Calf thymus DNA was obtained from Sigma, and pUC19 DNA was supplied by Genetix Biotech. Cu(OAc)$_2$·H_2O (GR), 1,10-phenanthroline monohydrate, meth-

https://doi.org/10.1021/acsomega.1c05750
ACS Omega 2022, 7, 2881−2896

anol (GR), absolute ethanol, DMF (GR), and DMSO were purchased from Merck.

4.2. Preparation of the Schiff Base and Copper(II) Compound (1). *4.2.1. 1,5-Bis(salicylidene)-thiocarbohydrazide, (o-HOC$_6$H$_4$CH═NNH)$_2$C═S.* This Schiff base was prepared and characterized following the method already reported[53] by us. In brief, salicylaldehyde (5 mmol) was added directly to a solution of thiocarbohydrazide (2.5 mmol) in 50 mL of absolute ethanol and then stirred for 2 h at RT. A cream-colored solid was separated from the solution, collected by filtration, washed using ethanol, and then recrystallized from methanol. Yield: 68%; mp 191 °C. Anal. calcd for $C_{15}H_{14}N_4O_2S$: C 57.30, H 4.49, N 17.83%; Found: C 57.41, H 4.47, N 17.90%.

4.2.2. [Cu(HL)(o-phen)]·H$_2$O. A dark blue solution prepared by adding slowly and dropwise a methanol solution (10 mL) of 1,10-phenanthroline (0.2 g, 0.001 mol) to a methanol solution (15 mL) of $Cu(OAc)_2·H_2O$ (0.2 g, 0.001 mol) was added to a methanol solution (30 mL) of $(o\text{-}HOC_6H_4CH{=}NNH)_2C{=}S$ (0.157 g, 0.0005 mol) for 20 min at RT and stirred for 3 h, and the brown-green solid that separated was filtered, washed thoroughly with methanol, and dried. It was then recrystallized from the CH_3CN solution. Yield ∼ 65%. Anal. calcd for $C_{27}H_{20}O_3N_6SCu$: C 56.68, H 3.52, N 14.69, Cu 11.11%; Found: C 57.06, H 3.59, N 14.82, Cu 11.03%. ESI-MS in CH_3CN: m/z 391.02 $[M - (o\text{-phen})]^+$ corresponds to $[Cu(HL)(H_2O)]^+$ or $[Cu(C_{15}H_{10}N_4O_2S)(H_2O)]^+$; m/z 181.07 $[(o\text{-phen}) + H]^+$ corresponds to $[C_{12}H_8N_2 + H]^+$; m/z 313.07 $[H_3L + H]^+$ corresponds to $[C_{15}H_{12}N_4O_2S + H]^+$.

Single crystals of this compound were obtained within 3 months by slow evaporation of a saturated acetonitrile solution placed at 4 °C.

4.3. X-ray Crystallography. X-ray data for **1** (Table 6) was collected using a Bruker AXS D8 VENTURE diffractometer equipped with Mo (Kα) (λ = 0.71073 Å) radiation and a PHOTON II area detector. The unit cell was determined[53,75] by collecting reflections, and then, intensity data for determining the structure of **1** was collected, as described in refs 53 and 75. In brief, the frames were integrated using the program APEX3-SAINT,[55] absorption correction was performed using the program SADABS,[55] SHELXT-2018[56] was used to solve the structure, and it was refined by SHELXL-2018,[56] a computer program incorporated in the WinGX system version v2018.3. ORTEP3[57] was used to draw the molecular graphics. Other details are as described in refs 53 and 75.

Table 6. X-ray Diffraction (XRD) Data and Structure Refinement for Complex 1[a]

empirical formula	$C_{110}H_{81}Cu_4N_{25}O_{11}S_4$
formula weight	2311.39
temperature	296(2) K
wavelength	0.71073 Å
crystal system	monoclinic
space group	$P2_1/c$
unit cell dimensions	a = 14.1837(6) Å, α = 90°
	b = 30.1761(14) Å, β = 99.238(2)°
	c = 12.5658(6) Å, γ = 90°
volume	5308.5(4) Å^3
Z	2
density (calculated)	1.446 Mg/m^3
absorption coefficient	0.942 mm^{-1}
F(000)	2368
crystal size	0.250 × 0.200 × 0.150 mm^3
θ range for data collection	2.422−24.999°
index ranges	$-16 \le h \le 16$, $-35 \le k \le 35$, $-14 \le l \le 14$
reflections collected	114 330
independent reflections	9327 [R(int) = 0.0781]
completeness to θ = 24.999°	99.8%
absorption correction	semi-empirical from equivalents
max. and min. transmission	0.7457 and 0.6626
refinement method	full-matrix least-squares on F^2
data/restraints/parameters	9327/35/718
goodness of fit on F^2	1.165
final R indices [$I > 2\sigma(I)$]	R_1 = 0.0876, wR_2 = 0.1909
R indices (all data)	R_1 = 0.1118, wR_2 = 0.2032
extinction coefficient	n/a
largest diff. peak and hole	0.822 and −0.645 e Å^{-3}

[a]CCDC number obtained from the Cambridge Crystallographic Data Center for the compound is 2110781.

4.4. DNA Binding Studies. *4.4.1. Electronic Spectroscopic Analysis.* The DNA binding experiment for **1** was done with a Jasco spectrophotometer using CT-DNA after checking its purity of CT-DNA and calculating its concentration as described.[53] The electronic absorption titration experiments were carried out by varying the CT-DNA concentration from 0 to 15 μM in 10 mM Tris−HCl buffer (pH 7.45) but keeping the concentration of **1** fixed at 5 × 10^{-5} M. The K_b was calculated from absorption titration data employing the Wolfe−Shimer equation.

4.4.2. Ethidium Bromide Displacement Experiment. Ethidium bromide (EB) does not have any fluorescence property in Tris−HCl, but when a solution having 50 μM CT-DNA and 2 μM EB was incubated in 10 mM Tris−HCl buffer (pH = 8) and allowed to stand, EB undergoes intercalative binding to DNA and the EB-bound CT-DNA showed enhanced fluorescence. To this DNA/EB mixture when incremental amounts of complex **1** (0−37.5 μM) were added, it led to a reduction in the fluorescence emission intensity owing to a competitive interaction of the metal complex and displacement of the bound ethidium bromide. Experiments were done employing a Jasco spectrofluorometer FP-8500 at an excitation wavelength of 510 nm.

4.5. DNA Cleavage Studies. *4.5.1. DNA Cleavage under Hydrolytic and Oxidative Conditions.* Gel electrophoresis was used for the DNA cleavage following both hydrolytic and oxidative pathways.[53] In hydrolytic cleavage experiments, supercoiled pUC19 DNA (200 ng) was treated with different concentrations of complex **1** (0−250 μM). Each of the reaction mixture (total volume of 10 μL using Tris−HCl buffer (50 mM) having pH 8.0) was incubated at 37 °C for 3 h, and the reaction was then quenched by adding loading buffer containing 25% bromophenol blue, 0.25% xylene cyanol, and 30% glycerol and subsequently loaded onto 1% agarose gel. Electrophoresis was performed at 60 V for 1 h to ensure that bromophenol blue traveled 75% of the gel. This gel was stained using ethidium bromide (0.5 μg/mL), and the plasmid bands were visualized by viewing the gel under UV light. The bands were quantified using ImageJ to study the conversion of SC DNA (form I) to NC (form II).

Similarly, oxidative DNA cleavage was performed using supercoiled pUC19 DNA (200 ng), and varying concentrations of complex **1** (0−10 μM) were added in the presence

https://doi.org/10.1021/acsomega.1c05750
ACS Omega 2022, 7, 2881−2896

of 1 mM hydrogen peroxide, which was used as an oxidizing agent; the reaction mixture was incubated at 37 °C for 1 h in the dark, then electrophoresis was performed at 60 V for 1 h, and the cleaved DNA products were analyzed. Further, experiments were also done after adding 2 μL of DMSO ($OH^{\bullet}$ scavenger) or 500 μM NaN_3 (singlet oxygen quencher). These scavenging agents were added before adding complex **1** to pUC19 DNA.

4.6. Interaction Studies with HSA. *4.6.1. Fluorescence Quenching Experiments.* Fluorescence spectra were recorded at room temperature (25 °C) with a Jasco fluorescence spectrophotometer model FP-8500 using quartz cells (1.0 cm). The spectrum of 4 μM HSA was scanned in the 300−420 nm range (λ_{ex} = 295 nm), and the maximum was observed at around 345 nm. Thereafter, incremental amounts (increment of 2 μM) of complex **1** were added and the spectra were collected to monitor the quenching effect of the complex on the fluorescence intensity. The experimental data was used to draw the Stern−Volmer plot, and the quenching parameters were then calculated from Stern−Volmer and modified Stern−Volmer equations.

4.6.2. Synchronous and 3D Fluorescence Experiments. Synchronous spectra were measured to study changes in the hydrophobic microenvironment around tyrosine and tryptophan amino acid residues of HSA. To a 4 μM solution of HSA in sodium phosphate buffer (20 mM) having pH 7.4, complex **1** was added in varying concentrations (increment of 2 μM). The fluorescence quenching curves were recorded in emission wavelengths in the 260−340 nm range with $\Delta\lambda$ = 15 nm and in the 280−400 nm range with $\Delta\lambda$ = 60 nm (where $\Delta\lambda = \lambda_{em} - \lambda_{ex}$). The 3D spectra were monitored with 4 μM HSA in the absence and presence of 4 μM complex **1** in the 230−500 nm range using λ_{ex} = 220 nm, successive increment = 10 nm, and slit opening = 5 nm.

4.6.3. UV−Vis Spectroscopy. The electronic spectrum of HSA (4 μM) solution (pH = 7.4) in sodium phosphate buffer (20 mM) was recorded at RT (25 °C) in the wavelength range of 500−200 nm. To assess the influence of the complex on the secondary conformation of HSA, **1** (4 μM) was added into sample and reference cuvettes (to nullify absorption due to the free complex) and spectra were recorded.

4.6.4. FRET Measurements. The separation distance between the donor and the acceptor was determined using FRET. For this, the electronic spectrum of **1** (4 μM) and the fluorescence spectrum of HSA (4 μM) were recorded in the wavelength region of 300−450 nm. A plot of the normalized emission intensity of HSA ($\overline{I}_D(\lambda)$) along with the extinction coefficient of **1** ($\varepsilon_A(\lambda)$) in the wavelength range 300−450 nm was used to determine the overlap integral J and the Förster distance *r*.

4.7. Molecular Docking. Protein-ligand docking helped us to characterize the behavior of small molecules by studying their binding at various sites of the targeted protein molecule. In this work, AutoDock Vina Software was used to perform the computation simulation of docking to analyze the nature of complex **1** binding with HSA. Data for the HSA crystal structure (PDB IB: 1H9Z) obtained from the Protein Data Bank was used in this study. The Gromacs molecular dynamics (MD) simulation package was used to perform the energy minimization process with the HSA molecule. During the energy minimization process, hydrogen atoms were added to the HSA structure after removing water molecules. MD simulations were performed for 500 000 steps with a 0.002 fs time step with the NVT ensemble. The modified Berendsen thermostat was used to keep the temperature constant. The crystallographic information file format (.CIF) of metal complex **1** is converted to the .pdbqt file format for continuing the docking simulation process. A 94 × 56 × 96 grid box was designed, and the calculation was performed as described in ref 53. A total of 100 runs were performed to obtain the possible conformations of binding. The lowest binding energy obtained from the docking simulation was −11.2 kcal/mol. The binding energy for iterations in each run ranges between −8.5 and −11.2 kcal/mol. Thus, the structures with the lowest energy were obtained from the calculations of the docking experiments. For getting output and analyzing H-bonds, PyMOL software was used.[53]

4.8. In Vitro Anticancer Studies. *4.8.1. Cell Viability Assay.* The cell viability assay was carried out to see the effect of metal complex **1** on cell proliferation using yellow 3-(4,5-dimethylthiazol-2-yl)-2,5-diphenyltetrazolium bromide (MTT). which is converted into purple formazan by mitochondrial reductase, and this activity was monitored. In brief, the cultured and seeded HeLa cells and MCF7 cells at a density of 2 × 10^4 in a 96-well plate were treated with 0.5, 1, 2.5, 5, and 10 μM complex **1** and incubated for 24 h. Along with treated cells, controls comprising of untreated cells were also maintained under the same condition. Afterward, the medium was removed and the cells were incubated for 4 h at 37 °C after adding 100 μL of MTT (5 mg/mL) to each well. The formazan crystals formed were dissolved using 100 μL of DMSO, and the absorbance was measured at 570 nm using an ELISA plate reader. The absorbance given by untreated cells was considered as 100% cell survival. The MTT assay was also performed by the same method using the HaCaT cell line to see the effect of **1** on noncancerous cells. In addition, to compare the results of **1** with cisplatin, the cytotoxic effect of cisplatin was also studied under the same experimental condition.

Statistical analysis of the results obtained from the MTT assay for **1** in HeLa and MCF7 cells was performed with GraphPad Prism 8.4.3 software using one-way ANOVA. $P < 0.05$ values were considered to be statistically significant.

4.8.2. Nuclear Staining. In this assay, Hoechst 33342 was used for DNA staining to observe nuclear morphological changes. Briefly, HeLa cells grown at a density of 5 × 10^5 cells per well on a coverslip in a six-well plate were incubated with the IC_{50} dose of **1** (except control cells) at 37 °C for 24 h. Afterward, the fluorescence microscopy was performed following the protocol described in ref 53.

4.8.3. Acridine Orange/Propidium Iodide (AO/PI) Double Staining. The morphological images during apoptosis were studied using AO/PI dye. In a six-well plate, HeLa cells were plated at a density of 5 × 10^5 cells/well. After 24 h incubation at 37 °C, they were treated with varying doses (0.5, 0.7, 1.0, and 1.5 μM) of complex **1** and incubated. After 24 h of incubation, the medium was removed and the cells were rinsed twice with phosphate-buffered saline (1× PBS); subsequently, the cells were stained using 20 μM 1:1 AO/PI mixture, incubated in the dark at 37 °C for 30 min, washed again with 1× PBS, and then analyzed by viewing under a fluorescence microscope.

4.8.4. Detection of Intracellular ROS. ROS generation was monitored using nonfluorescent probe 2′,7′-dichloro-dihydro-fluorescein-diacetate (H_2DCFDA). Briefly, HeLa cells seeded at a density of 5 × 10^5 cells per well in a six-well plate were

https://doi.org/10.1021/acsomega.1c05750
ACS Omega 2022, 7, 2881−2896

then treated with complex **1** (0.5, 0.75, 1.0, 1.5 μM) for 6 h in a CO_2 incubator at 37 °C, while untreated cells were kept as the control. After washing the treated cells with PBS, these were resuspended in 10 μM H_2DCFDA and kept at 37°C for 30 min. Finally, they were washed twice using PBS and viewed under a fluorescence microscope. The fluorescence was measured at 530 nm using λ_{ex} = 485 nm. *tert*-Butyl hydrogen peroxide (*t*-BHP, 25 μM) was used as the positive control.

4.8.5. Cell Cycle Arrest. Cell cycle progression was determined by flow cytometric analysis. HeLa cells were plated in a six-well plate at a density of 1×10^6 cells/well for 24 h and then treated with various doses (0.5, 1.5, 2.5, 5 μM) of **1** for another 24 h. Cells were trypsinized, collected, fixed with chilled 70% ethanol, and incubated for 15 min. After centrifugation and discarding the supernatant, cells were suspended in 50 μL of 1× PBS and then stained with PI (300 μL of 50 μg/mL) along with the treatment of 10 μL (10 μg) of RNase from the stock of 1 mg/mL. It was incubated on ice for 30 min. Flow cytometry was used to measure the DNA content with the help of BD FACS Melody, and then, cell cycle distribution was obtained after appropriate gating of the cell population.

4.9. Physical Measurements. Microanalyses were done using a PerkinElmer model 2400 series II CHNS/O analyzer. Copper was estimated iodometrically using a standardized sodium thiosulphate solution. Mass spectra were recorded with a Thermo Scientific Q Exactive hybrid quadrupole-orbitrap mass spectrometer. A Shimadzu IR Affinity - 1 FT-IR spectrometer was used for recording IR spectra using the KBr pellet, while a Jasco V-570 UV/Vis/NIR spectrophotometer was employed for recording electronic absorption spectra at RT (25 °C) using a pair of quartz cells having a 1 cm path length. A JEOL model JES-FA200 ESR spectrometer was used for recording X-band electron paramagnetic resonance (EPR) spectra at RT and LNT. An aqueous cell was used to record RT solution EPR spectra. The IVIUMSTAT (10 V/5 A/8 MHz) electrochemical workstation was used for electrochemical experiments using a conventional three-electrode cell[53] (a platinum working electrode, a Ag/AgCl reference electrode, and a platinum auxiliary electrode) under an inert atmosphere and in the presence of supporting electrolyte ($[N(n\text{-}Bu)_4]ClO_4$). A Jasco spectrofluorometer model FP-8500 was used for fluorescence spectrum measurements, and a Bruker Axs Kappa Apex2 diffractometer was used for X-ray crystal structure determination.

■ ASSOCIATED CONTENT

Supporting Information

The Supporting Information is available free of charge at https://pubs.acs.org/doi/10.1021/acsomega.1c05750.

ESI-MS spectrum of **1** in CH_3CN (Figure S1), IR spectra of 1,5-bis(salicylidene)thiocarbohydrazide and **1** (Figure S2), electronic spectrum of **1** (Figure S3), X-band EPR spectra of **1** (Figure S4), cyclic voltammogram of **1** in DMF (Figure S5), electronic spectrum of HSA (4 μM) (Figure S6), MTT assay of HaCaT with different doses of **1** for 24 h (Figure S7), MTT assay showing cell viability of HeLa and MCF7 cells with different doses of cisplatin for 24 h (Figure S8), results of the AO/PI staining assay of HeLa cells with **1** (0.5, 0.7, 1.0, and 1.5 μM) for 24 h (Figure S9), detection of intracellular ROS using H_2DCFDA (10 μM) in HeLa cells (Figure S10), effect of **1** on cell cycle progression in HeLa cells (Figure S11) (PDF)

Accession Codes

CCDC number is 2110781 for compound **1**.

■ AUTHOR INFORMATION

Corresponding Author

Manjuri Kumar − *Department of Chemical Engineering, Birla Institute of Technology and Science-Pilani, Zuarinagar 403726 Goa, India;* orcid.org/0000-0002-8102-8923; Email: manjuri@goa.bits-pilani.ac.in

Authors

Sidhali U. Parsekar − *Department of Chemical Engineering, Birla Institute of Technology and Science-Pilani, Zuarinagar 403726 Goa, India*

Kumudini Paliwal − *Department of Chemical Engineering, Birla Institute of Technology and Science-Pilani, Zuarinagar 403726 Goa, India*

Paramita Haldar − *Department of Chemical Engineering, Birla Institute of Technology and Science-Pilani, Zuarinagar 403726 Goa, India*

P. K. Sudhadevi Antharjanam − *Sophisticated Analytical Instrument Facility, Indian Institute of Technology—Madras, Chennai 600036, India;* orcid.org/0000-0002-8801-7530

Complete contact information is available at: https://pubs.acs.org/10.1021/acsomega.1c05750

Author Contributions

§S.U.P. and K.P. contributed equally to this work.

Notes

The authors declare no competing financial interest.

■ ACKNOWLEDGMENTS

M.K. thanks SERB, Department of Science and Technology (DST), New Delhi, Govt. of India for project EMR/2017/001562. Facilities provided by SAIF, IIT-Madras for XRD; SAIF, IIT-Bombay for EPR; and the CSIR-National Chemical Laboratory (NCL), Pune for high-resolution mass spectrum of the compound are gratefully acknowledged. The authors also thank the Department of Biological Sciences, Birla Institute of Technology and Science Pilani, K. K. Birla Goa Campus for providing facilities for cell culture and cell cycle analysis. The authors also thank CSIF of our Institute for providing instrumental facilities.

■ REFERENCES

(1) Santini, C.; Pellei, M.; Gandin, V.; Porchia, M.; Tisato, F.; Marzano, C. Advances in Copper Complexes as Anticancer Agents. *Chem. Rev.* **2014**, *114*, 815−862.

(2) Barone, G.; Terenzi, A.; Lauria, A.; Almerico, A. M.; Leal, J. M.; Busto, N.; García, B. DNA-binding of nickel(II), copper(II) and zinc(II) complexes: Structure−affinity relationships. *Coord. Chem. Rev.* **2013**, *257*, 2848−2862. and references therein.

(3) Rajalakshmi, S.; Kiran, M. S.; Nair, B. U. DNA condensation by copper (II) complexes and their anti-proliferative effect on cancerous and normal fibroblast cells. *Eur. J. Med. Chem.* **2014**, *80*, 393−406.

(4) Nagababu, P.; Barui, A. K.; Thulasiram, B.; Shobha Devi, C.; Satyanarayana, S.; Patra, C. R.; Sreedhar, B. Antiangiogenic activity of mononuclear copper(II) polypyridyl complexes for the treatment of cancers. *J. Med. Chem.* **2015**, *58*, 5226−5241.

(5) Anjomshoa, M.; Hadadzadeh, H.; Torkzadeh-Mahani, M.; Fatemi, S. J.; Adeli-Sardou, M.; Rudbari, H. A.; Nardo, V. M. A mononuclear Cu(II) complex with 5,6-diphenyl-3-(2-pyridyl)-1,2,4-triazine: Synthesis, crystal structure, DNA- and BSA-binding, molecular modeling, and anticancer activity against MCF-7, A-549, and HT-29 cell lines. *Eur. J. Med. Chem.* **2015**, *96*, 66−82.
(6) Adak, P.; Ghosh, B.; Bauza, A.; Frontera, A.; Blake, A. J.; Corbella, C. M.; Das-Mukhopadhyay, C.; Chattopadhyay, S. K. Catecholase activity, DNA binding and cytotoxicity studies of a Cu(II) complex of a pyridoxal Schiff base: Synthesis, X-ray crystal structure, spectroscopic, electrochemical and theoretical studies. *RSC Adv.* **2016**, *6*, 86851−86861.
(7) O'Connor, M.; Kellett, A.; McCann, M.; Rosair, G.; McNamara, M.; Howe, O.; Creaven, B. S.; McClean, S.; Foltyn-Arfa Kia, A.; O'Shea, D.; Devereux, M. Copper(II) complexes of salicylic acid combining superoxide dismutase mimetic properties with DNA binding and cleaving capabilities display promising chemotherapeutic potential with fast acting in vitro cytotoxicity against cisplatin sensitive and resistant cancer cell lines. *J. Med. Chem.* **2012**, *55*, 1957−1968.
(8) Rajalakshmi, S.; Weyhermüller, T.; Dinesh, M.; Nair, B. U. Copper (II) complexes of terpyridine derivatives: A footstep towards development of antiproliferative agent for breast cancer. *J. Inorg. Biochem.* **2012**, *117*, 48−59.
(9) Maheswari, P. U.; Roy, S.; den Dulk, H.; Barends, S.; van Wezel, G.; Kozlevčar, B.; Gamez, P.; Reedijk, J. The square-planar cytotoxic [CuII(pyrimol)Cl] complex acts as an efficient DNA cleaver without reductant. *J. Am. Chem. Soc.* **2006**, *128*, 710−711.
(10) Zhang, Y.; Zhang, L.; Liu, L.; Guo, J.; Wua, D.; Xu, G.; Wang, X.; Jia, D. Anticancer activity, structure, and theoretical calculation of N-(1-phenyl-3-methyl-4-propyl-pyrazolone-5)-salicylidene hydrazone and its copper(II) complex. *Inorg. Chim. Acta* **2010**, *363*, 289−293.
(11) Wang, J. T.; Xia, Q.; Zheng, X. H.; Chen, H. Y.; Chao, H.; Mao, Z. W.; Ji, L. N. An effective approach to artificial nucleases using copper(II) complexes bearing nucleobases. *Dalton Trans.* **2010**, *39*, 2128−2136.
(12) Dhar, S.; Reddy, P. A.; Chakravarty, A. R. Intramolecular nucleophilic activation promoting efficient hydrolytic cleavage of DNA by (aqua)bis-(dipyridoquinoxaline)copper(II) complex. *Dalton Trans.* **2004**, 697−698.
(13) Zhang, C. X.; Lippard, S. J. New metal complexes as potential therapeutics. *Currn. Opin. Chem. Biol.* **2003**, *7*, 481−489.
(14) Qiao, X.; Ma, Z.-Y.; Xie, C.-Z.; Xue, F.; Zhang, Y.-W.; Xu, J.-Y.; Qiang, Z.-Y.; Lou, J.-S.; Chen, G.-J.; Yan, S.-P. Study on potential antitumor mechanism of a novel Schiff base copper(II) complex: synthesis, crystal structure, DNA binding, cytotoxicity and apoptosis induction activity. *J. Inorg. Biochem.* **2011**, *105*, 728−737.
(15) Tardito, S.; Basanetti, I.; Bignardi, C.; Elviri, L.; Tegoni, M.; Mucchino, C.; Bussolati, O.; Franchi-Gazzola, R.; Marchio, L. Copper binding agents acting as copper ionophores lead to caspase inhibition and paraptotic cell death in human cancer cells. *J. Am. Chem. Soc.* **2011**, *133*, 6235−6242.
(16) Goswami, T. K.; Chakravarthi, B. V. S. K.; Roy, M.; Karande, A. A.; Chakravarty, A. R. Ferrocene-conjugated L-tryptophan copper(II) complexes of phenanthroline bases showing DNA photocleavage activity and cytotoxicity. *Inorg. Chem.* **2011**, *50*, 8452−8464.
(17) Senthil Raja, D.; Paramaguru, G.; Bhuvanesh, N. S. P.; Reibenspies, J. H.; Renganathan, R.; Natarajan, K. Effect of terminal N-substitution in 2-oxo-1,2-dihydroquinoline-3-carbaldehyde thiosemicarbazones on the mode of coordination, structure, interaction with protein, radical scavenging and cytotoxic activity of copper(II) complexes. *Dalton Trans.* **2011**, *40*, 4548−4559.
(18) Devereux, M.; Shea, D. O.; Kellett, A.; McCann, M.; Walsh, M.; Egan, D.; Deegan, C.; Kedziora, K.; Rosair, G.; Muller-Bunz, H. Synthesis, X-ray crystal structures and biomimetic and anticancer activities of novel copper(II)benzoatecomplexes incorporating 2-(4′-thiazolyl)- benzimidazole(thiabendazole), 2-(2-pyridyl)benzimidazole and 1,10-phenanthrolineas chelating nitrogen donor ligands. *J. Inorg. Biochem.* **2007**, *101*, 881−892.
(19) Desbouis, D.; Troitsky, I. P.; Belousoff, M. J.; Spiccia, L.; Graham, B. Copper(II), zinc(II) and nickel(II) complexes as nuclease mimetics. *Coord. Chem. Rev.* **2012**, *256*, 897−937.
(20) Rosu, T.; Pahontu, E.; Pasculescu, S.; Georgescu, R.; Stanica, N.; Curaj, A.; Popescu, A.; Leabu, M. Synthesis, characterization antibacterial and antiproliferative activity of novel Cu(II) and Pd(II) complexes with 2-hydroxy-8-R-tricyclo[7.3.1.0.(2,7)]tridecane-13-one thiosemicarbazone. *Eur. J. Med. Chem.* **2010**, *45*, 1627−1634.
(21) Lahiri, D.; Majumdar, R.; Mallick, D.; Goswami, T. K.; Dighe, R. R.; Chakravarty, A. R. Remarkable photocytotoxicity in hypoxic HeLa cells by a dipyridophenazine copper(II) Schiff base thiolate. *J. Inorg. Biochem.* **2011**, *105*, 1086−1094.
(22) Barve, A.; Kumbhar, A.; Bhat, M.; Joshi, B.; Butcher, R.; Sonawane, U.; Joshi, R. Mixed-ligand copper(II) maltolate complexes: synthesis, characterization, DNA binding and cleavage, and cytotoxicity. *Inorg. Chem.* **2009**, *48*, 9120−9132.
(23) García-Ramos, J. C.; Toledano-Magana, Y.; Talavera-Contreras, L. G.; Flores-Alamo, M.; Ramirez-Delgado, V.; Morales-Leon, E.; Ortiz-Frade, L.; Gutierrez, A. G.; Vazquez-Aguirre, A.; Mejia, C.; Carrero, J. C.; Laclette, J. P.; Moreno-Esparza, R.; Ruiz-Azuara, L. Potential cytotoxic and amoebicide activity of first row transition metal compounds with 2,9-bis-(2′,5′-diazahexanyl)-1,1-phenanthroline (L1). *Dalton Trans.* **2012**, *41*, 10164−10174.
(24) Abdi, K.; Hadadzadeh, H.; Weil, M.; Salimi, M. Mononuclear copper(II) complex with terpyridine and an extended phenanthroline base, $[Cu(tpy)(dppz)]^{2+}$: Synthesis, crystal structure, DNA binding and cytotoxicity activity. *Polyhedron* **2012**, *31*, 638−648.
(25) Manan, M. A. F. A.; Tahir, M. I. M.; Crouse, K. A.; Rosli, R.; How, F. N. F.; Watkin, D. J. The crystal structure and cytotoxicity of centrosymmetric copper(II) complex derived from S-methyldithiocarbazate with isatin. *J. Chem. Crystallogr.* **2011**, *41*, 1866−1871.
(26) Zhou, X.-Q.; Li, Y.; Zhang, D.-Y.; Nie, Y.; Li, Z.-J.; Gu, W.; Liu, X.; Tian, J.-L.; Yan, S.-P. Copper complexes based on chiral Schiff-base ligands: DNA/BSA binding ability, DNA cleavage activity, cytotoxicity and mechanism of apoptosis. *Eur. J. Med. Chem.* **2016**, *114*, 244−256.
(27) Hu, K.; Liu, C.; Lia, J.; Liang, F. Copper(II) complexes based on quinoline-derived Schiff-base ligands: synthesis, characterization, HSA/DNA binding ability, and anticancer activity. *Med. Chem. Commun.* **2018**, *9*, 1663−1672.
(28) Dankhoff, K.; Gold, M.; Kober, L.; Schmitt, F.; Pfeifer, L.; Dürrmann, A.; Kostrhunova, H.; Rothemund, M.; Brabec, V.; Schobert, R.; Weber, B. Copper(II) complexes with tridentate Schiff base-like ligands: solid state and solution structures and anticancer activity. *Dalton Trans.* **2019**, *48*, 15220−15230.
(29) Kordestani, N.; Rudbari, H. A.; Fernandes, A. R.; Raposo, L. R.; Luz, A.; Baptista, P. V.; Bruno, G.; Scopelliti, R.; Fateminia, Z.; Micale, N.; Tumanov, N.; Wouters, J.; Kajanif, A. A.; Bordbar, A.-K. Copper(II) complexes with tridentate halogen-substituted Schiff base ligands: synthesis, crystal structures and investigating the effect of halogenation, leaving groups and ligand flexibility on antiproliferative activities. *Dalton Trans.* **2021**, *50*, 3990−4007.
(30) Molinaro, C.; Martoriati, A.; Pelinski, L.; Cailliau, K. Copper complexes as anticancer agents targeting topoisomerases I and II. *Cancers* **2020**, *12*, No. 2863.
(31) Rostas, A. M.; Badea, M.; Ruta, L. L.; Farcasanu, I. C.; Maxim, C.; Chifiriuc, M. C.; Popa, M.; Luca, M.; Korosin, N. C.; Korosec, R. C.; Bacalum, M.; Raileanu, M.; Olar, R. Copper(II) complexes with mixed heterocycle ligands as promising antibacterial and antitumor species. *Molecules* **2020**, *25*, No. 3777.
(32) Jamieson, E. R.; Lippard, S. J. Structure, recognition, and processing of cisplatin−DNA adducts. *Chem. Rev.* **1999**, *99*, 2467−2498.
(33) Wang, D.; Lippard, S. J. Cellular processing of platinum anticancer drugs. *Nat. Rev. Drug Discovery* **2005**, *4*, 307−320.
(34) Todd, R. C.; Lippard, S. J. Inhibition of transcription by platinum antitumor compounds. *Metallomics* **2009**, *1*, 280−291.

https://doi.org/10.1021/acsomega.1c05750
ACS Omega 2022, 7, 2881−2896

(35) Johnstone, T. C.; Park, G. Y.; Lippard, S. J. Understanding and improving platinum anticancer drugs − phenanthriplatin. *Anticancer Res.* **2014**, *34*, 471−476.
(36) Johnstone, T. C.; Suntharalingam, K.; Lippard, S. J. The next generation of platinum drugs: Targeted Pt(II) agents, nanoparticle delivery, and Pt(IV) prodrugs. *Chem. Rev.* **2016**, *116*, 3436−3486.
(37) Wheate, N. J.; Walker, S.; Craig, G. E.; Oun, R. The status of platinum anticancer drugs in the clinic and in clinical trials. *Dalton Trans.* **2010**, *39*, 8113−8127.
(38) Galanski, M.; Keppler, B. K. Searching for the magic bullet: Anticancer platinum drugs which can be accumulated or activated in the tumor tissue. *Anti-Cancer Agents Med. Chem.* **2007**, *7*, 55−73.
(39) Kelland, L. The resurgence of platinum-based cancer chemotherapy. *Nat. Rev. Cancer.* **2007**, *7*, 573−584.
(40) Hambley, T. W. Metal-based therapeutics. *Science* **2007**, *318*, 1392−1393.
(41) Qin, Q.-P.; Wang, Z.-F.; Huang, X.-L.; Tan, M.-X.; Zou, B.-Q.; Liang, H. In vitro and in vivo antitumor activities of three novel binuclear platinum(II) complexes with 4′-substituted-2,2′:6′,2″-terpyridine ligands. *Eur. J. Med. Chem.* **2019**, *184*, No. 111751.
(42) Wang, X.; Wang, X.; Jin, S.; Muhammad, N.; Guo, Z. Stimuli-responsive therapeutic metallodrugs. *Chem. Rev.* **2019**, *119*, 1138−1192.
(43) Kratz, F.; Beyer, U. Serum proteins as drug carriers of anticancer agents: A review. *Drug Delivery* **1998**, *5*, 281−299.
(44) Hummer, A. A.; Bartel, C.; Arion, V. B.; Jakupec, M. A.; Meyer-Klaucke, W.; Geraki, T.; Quinn, P. D.; Mijovilovich, A.; Keppler, B. K.; Rompel, A. X-ray absorption spectroscopy of an investigational anticancer gallium(III) drug: Interaction with serum proteins, elemental distribution pattern, and coordination of the compound in tissue. *J. Med. Chem.* **2012**, *55*, 5601−5613.
(45) Dömötör, O.; Hartinger, C. G.; Bytzek, A. K.; Kiss, T.; Keppler, B. K.; Enyedy, E. A. Characterization of the binding sites of the anticancer ruthenium(III) complexes KP1019 and KP1339 on human serum albumin via competition studies. *J. Biol. Inorg. Chem.* **2013**, *18*, 9−17.
(46) Samari, F.; Hemmateenejad, B.; Shamsipur, M.; Rashidi, M.; Samouei, H. Affinity of two novel five-coordinated anticancer Pt(II) complexes to human and bovine serum albumins: a spectroscopic approach. *Inorg. Chem.* **2012**, *51*, 3454−3464.
(47) Shen, F.; Ou, Z. B.; Liu, Y. J.; Liu, W.; Wang, B. F.; Mao, Z. W.; Le, X. Y. Two Cu(II) complexes containing 2,4-diamino-6-(2-pyridyl)-1,3,5-triazine and amino acids: Synthesis, crystal structures, DNA/HSA binding, molecular docking, and *in vitro* cytotoxicity studies. *Inorg. Chim. Acta* **2017**, *465*, 1−13.
(48) Shen, F.; Liu, Y. X.; Li, S. M.; Jiang, C. K.; Wang, B. F.; Xiong, Y. H.; Mao, Z. W.; Le, X. Y. Synthesis, crystal structures, molecular docking and in vitro cytotoxicity studies of two new copper(II) complexes: special emphasis on their binding to HSA. *New J. Chem.* **2017**, *41*, 12429−12441.
(49) Qi, J.; Zhang, Y.; Gou, Y.; Zhang, Z.; Zhou, Z.; Wu, X.; Yang, F.; Liang, H. Developing an anticancer copper(II) pro-drug based on the His242 residue of the human serum albumin carrier IIA subdomain. *Mol. Pharm.* **2016**, *13*, 1501−1507.
(50) Enyedy, É. A.; Dömötör, O.; Bali, K.; Hetényi, A.; Tuccinardi, T.; Keppler, B. K. Interaction of the anticancer gallium(III) complexes of 8-hydroxyquinoline and maltol with human serum proteins. *J. Biol. Inorg. Chem.* **2015**, *20*, 77−88.
(51) Bijelic, A.; Theiner, S.; Keppler, B. K.; Rompel, A. X-ray structure analysis of indazolium *trans*-[tetrachlorobis(1*H*-indazole)-ruthenate(III)] (KP1019) bound to human serum albumin reveals two ruthenium binding sites and provides insights into the drug binding mechanism. *J. Med. Chem.* **2016**, *59*, 5894−5903.
(52) Hoogenboezem, E. N.; Duvall, C. L. Harnessing albumin as a carrier for cancer therapies. *Adv. Drug. Delivery Rev.* **2018**, *130*, 73−89.
(53) Parsekar, S. U.; Haldar, P.; Sudhadevi Antharjanam, P. K.; Kumar, M.; Koley, A. P. Synthesis, characterization, crystal structure, DNA and human serum albumin interactions, as well as antiproliferative activity of a Cu(II) complex containing a Schiff base ligand formed in situ from the Cu(II)-induced cyclization of 1,5-bis(salicylidene)thiocarbohydrazide. *Appl. Organomet. Chem.* **2021**, *35*, No. e6152.
(54) Bustos, C.; Burckhardt, O.; Schrebler, R.; Carrillo, D.; Arif, A. M.; Cowley, A. H.; Nunn, C. M. Synthesis, characterization, and electrochemistry of cis-dioxomolybdenum(VI) complexes of Schiff bases derived from carbohydrazide, thiocarbohydrazide, and salicylaldehyde. Crystal structures of $[MoO_2(o\text{-}OC_6H_4CH{:}NN{:}CSNHN{:}CHC_6H_4OH\text{-}o)Me_2SO]$ and $[(MoO_2)_2(o\text{-}OC_6H_4CH{:}NN{:}CONN{:}CHC_6H_4O\text{-}o)(Me_2SO)_2]$.cntdot.0.5$Me_2SO$. *Inorg. Chem.* **1990**, *29*, 3996−4001.
(55) *Apex3 v2017.3-0, SAINT V8.38A*; Bruker AXS Inc: Madison (WI), USA, 2016, 2013/2014.
(56) Sheldrick, G. M. *SHELXL-2018*; University of Göttingen: Germany, 2018.
(57) Farrugia, L. J. *ORTEP*-3 for Windows - a version of *ORTEP*-III with a Graphical User Interface (GUI). *J. Appl. Crystallogr.* **1997**, *30*, 565.
(58) Wolfe, A.; Shimer, G. H., Jr.; Meehan, T. Polycyclic aromatic hydrocarbons physically intercalate into duplex regions of denatured DNA. *Biochemistry* **1987**, *26*, 6392−6396.
(59) Wilson, W. D.; Ratmeyer, L.; Zhao, M.; Strekowski, L.; Boykin, D. The search for structure-specific nucleic acid-interactive drugs: effects of compound structure on RNA versus DNA interaction strength. *Biochemistry* **1993**, *32*, 4098−4104.
(60) Kelly, J. M.; Tossi, A. B.; McConnell, D. J.; OhUigin, C. A study of the interactions of some polypyridylruthenium (II) complexes with DNA using fluorescence spectroscopy, topoisomerisation and thermal denaturation. *Nucleic Acids Res.* **1985**, *13*, 6017−6034.
(61) Lakowicz, J. R.; Weber, G. Quenching of fluorescence by oxygen. Probe for structural fluctuations in macromolecules. *Biochemistry* **1973**, *12*, 4161−4170.
(62) Rajendiran, V.; Karthik, R.; Palaniandavar, M.; Stoeckli-Evans, H.; Periasamy, V. S.; Akbarsha, M. A.; Srinag, B. S.; Krishnamurthy, H. Mixed-ligand copper (II)-phenolate complexes: effect of coligand on enhanced DNA and protein binding, DNA cleavage, and anticancer activity. *Inorg. Chem.* **2007**, *46*, 8208−8221.
(63) Liu, J.; Zhang, T.; Lu, T.; Qu, L.; Zhou, H.; Zhang, Q.; Ji, L. DNA-binding and cleavage studies of macrocyclic copper (II) complexes. *J. Inorg. Biochem.* **2002**, *91*, 269−276.
(64) Sangeetha Gowda, K. R.; Mathew, B. B.; Sudhamani, C. N.; Bhojya Naik, H. S. Mechanism of DNA binding and cleavage. *J. Biomed. Biotechnol.* **2014**, *2*, 1−9.
(65) Li, W.; Zhou, P.; Zhang, J.; Zhang, Y.; Zhang, G.; Liu, Y.; Cheng, X. Generation of reactive oxygen species by promoting the Cu (II)/Cu (I) redox cycle with reducing agents in aerobic aqueous solution. *Water Sci. Technol.* **2018**, *78*, 1390−1399.
(66) Reddy, P. A.; Nethaji, M.; Chakravarty, A. R. Hydrolytic cleavage of DNA by ternary amino acid Schiff base copper (II) complexes having planar heterocyclic ligands. *Eur. J. Inorg. Chem.* **2004**, 1440−1446.
(67) Munteanu, A. C.; Badea, M.; Olar, R.; Silvestro, L.; Mihaila, M.; Brasoveanu, L. I.; Musat, M. G.; Andries, A.; Uivarosi, V. Cytotoxicity studies, DNA interaction and protein binding of new Al (III), Ga (III) and In (III) complexes with 5-hydroxyflavone. *Appl. Organomet. Chem.* **2018**, *32*, No. e4579.
(68) Shahabadi, N.; Fili, S. M.; Kashanian, M. Human serum albumin interaction studies of a new copper(II) complex containing ceftobiprole drug using molecular modeling and multispectroscopic methods. *J. Coord. Chem.* **2018**, *71*, 329−341.
(69) Hussain, A.; AlAjmi, M. F.; Rehman, M. T.; Amir, S.; Husain, F. M.; Alsalme, A.; Siddiqui, M. A.; AlKhedhairy, A. A.; Khan, R. A. Copper (II) complexes as potential anticancer and Nonsteroidal anti-inflammatory agents: In vitro and in vivo studies. *Sci. Rep.* **2019**, *9*, No. 5237.

https://doi.org/10.1021/acsomega.1c05750
ACS Omega 2022, 7, 2881−2896

(70) Basak, P.; Debnath, T.; Banerjee, R.; Bhattacharyya, M. Selective binding of divalent cations toward heme proteins. *Front. Biol.* **2016**, *11*, 32−42.
(71) Ali, M. S.; Al-Lohedan, H. A. Interaction of human serum albumin with sulfadiazine. *J. Mol. Liq.* **2014**, *197*, 124−130.
(72) Zhang, J.; Gao, X.; Huang, J.; Wang, H. Probing the Interaction between Human Serum Albumin and 9-Hydroxyphenanthrene: A spectroscopic and molecular docking study. *ACS Omega* **2020**, *5*, 16833−16840.
(73) Aseman, M. D.; Aryamanesh, S.; Shojaeifard, Z.; Hemmateenejad, B.; Nabavizadeh, S. M. Cycloplatinated(II) derivatives of mercaptopurine capable of binding interactions with HSA/DNA. *Inorg. Chem.* **2019**, *58*, 16154−16170.
(74) *FRET-Förster Resonance Energy Transfer: From Theory to Applications*; Medintz, I. L.; Hildebrandt, N., Eds.; John Wiley & Sons, 2013.
(75) Parsekar, S. U.; Velankanni, P.; Sridhar, S.; Haldar, P.; Mate, N. A.; Banerjee, A.; Sudhadevi Antharjanam, P. K.; Koley, A. P.; Kumar, M. Protein binding studies with human serum albumin, molecular docking and in vitro cytotoxicity studies using HeLa cervical carcinoma cells of Cu(II)/Zn(II) complexes containing a carbohydrazone ligand. *Dalton Trans.* **2020**, *49*, 2947−2965.
(76) Koley, M. K.; Parsekar, S. U.; Duraipandy, N.; Kiran, M. S.; Varghese, B.; Manoharan, P. T.; Koley, A. P. DNA binding and cytotoxicity of two Cu (II) complexes containing a Schiff base ligand along with 1, 10-phenanthroline or imidazole as a coligand. *Inorg. Chim. Acta* **2018**, *478*, 211−221.
(77) Al-Harthi, S.; Lachowicz, J. I.; Nowakowskia, M. E.; Jaremko, M.; Jaremko, Ł. Towards the functional high-resolution coordination chemistry of blood plasma human serum albumin. *J. Inorg. Biochem.* **2019**, *198*, No. 110716.
(78) Rahman, S.; Rehman, M. T.; Rabbani, G.; Khan, P.; AlAjmi, M. F.; Hassan, M.; Muteeb, G.; Kim, J. Insight of the interaction between 2,4-thiazolidinedione and human serum albumin: A spectroscopic, thermodynamic and molecular docking study. *Int. J. Mol. Sci.* **2019**, *20*, No. 2727.
(79) Zsila, F.; Bikadi, Z.; Malik, D.; Hari, P.; Pechan, I.; Berces, A.; Hazai, E. Evaluation of drug-human serum albumin binding interactions with support vector machine aided online automated docking. *Bioinformatics* **2011**, *27*, 1806−1813.
(80) Becit, M.; Aydin, S. An in vitro study on the interactions of pycnogenol with cisplatin in human cervical cancer cells. *Turkish J. Pharm. Sci.* **2020**, *17*, 1−6.
(81) Anbu, S.; Ravishankaran, R.; Karande, A. A.; Kandaswamy, M. DNA targeting polyaza macrobicyclic dizinc (II) complexes promoting high in vitro caspase dependent anti-proliferative activity against human carcinoma cancer cells. *Dalton Trans.* **2012**, *41*, 12970−12983.
(82) Lu, J.; Sun, Q.; Li, J. L.; Jiang, L.; Gu, W.; Liu, X.; Tian, J. L.; Yan, S. P. Two water-soluble copper (II) complexes: synthesis, characterization, DNA cleavage, protein binding activities and in vitro anticancer activity studies. *J. Inorg. Biochem.* **2014**, *137*, 46−56.
(83) Czarnomysy, R.; Bielawski, K.; Muszynska, A.; Bielawska, A.; Gornowicz, A. Biological evaluation of dimethylpyridine−platinum complexes with potent antiproliferative activity. *J. Enzyme Inhib. Med. Chem.* **2016**, *31*, 150−165.
(84) Suberu, J. O.; Romero-Canelón, I.; Sullivan, N.; Lapkin, A. A.; Barker, G. C. Comparative cytotoxicity of artemisinin and cisplatin and their interactions with chlorogenic acids in MCF7 breast cancer cells. *ChemMedChem* **2014**, *9*, 2791−2797.
(85) Manikandamathavan, V. M.; Weyhermüller, T.; Parameswari, R. P.; Sathishkumar, M.; Subramanian, V.; Nair, B. U. DNA/protein interaction and cytotoxic activity of imidazole terpyridine derived Cu (II)/Zn (II) metal complexes. *Dalton Trans.* **2014**, *43*, 13018−13031.
(86) Koley, M. K.; Duraipandy, N.; Kiran, M. S.; Varghese, B.; Manoharan, P. T.; Koley, A. P. DNA binding and cytotoxicity of some Cu (II)/Zn (II) complexes containing a carbohydrazone Schiff base ligand along with 1, 10-phenanthroline as a coligand. *Inorg. Chim. Acta* **2017**, *466*, 538−550.
(87) Recio Despaigne, A. A.; Da Silva, J. G.; Da Costa, P. R.; Dos Santos, R. G.; Beraldo, H. ROS-mediated cytotoxic effect of copper (II) hydrazone complexes against human glioma cells. *Molecules* **2014**, *19*, 17202−17220.
(88) Usman, M.; Arjmand, F.; Khan, R. A.; Alsalme, A.; Ahmad, M.; Tabassum, S. Biological evaluation of dinuclear copper complex/dichloroacetic acid cocrystal against human breast cancer: design, synthesis, characterization, DFT studies and cytotoxicity assays. *RSC Adv.* **2017**, *7*, 47920−47932.
(89) Zhao, W.; Feng, H.; Sun, W.; Liu, K.; Lu, J. J.; Chen, X. Tert-butyl hydroperoxide (t-BHP) induced apoptosis and necroptosis in endothelial cells: Roles of NOX4 and mitochondrion. *Redox Biol.* **2017**, *11*, 524−534.
(90) Han, Y. H.; Moon, H. J.; You, B. R.; Park, W. H. The effect of MG132, a proteasome inhibitor on HeLa cells in relation to cell growth, reactive oxygen species and GSH. *Oncol. Rep.* **2009**, *22*, 215−221.

https://doi.org/10.1021/acsomega.1c05750
ACS Omega 2022, 7, 2881−2896